

# Nuclear stellar discs in early-type galaxies — I. HST and WHT observations

Frank C. van den Bosch<sup>1,2</sup>, Walter Jaffe<sup>1</sup> and Roeland P. van der Marel<sup>3,4</sup>

<sup>1</sup> *Sterrewacht Leiden, Postbus 9513, 2300 RA Leiden, The Netherlands*

<sup>2</sup> *Astronomy Dept., University of Washington, P.O. Box 351580, Seattle WA 98195-1580, USA*

<sup>3</sup> *Institute for Advanced Study, Princeton, NJ 08540, USA*

<sup>4</sup> *Hubble Fellow*

## ABSTRACT

We present multi-colour ( $U$ ,  $V$  and  $I$ ) photometry obtained with the second Wide Field and Planetary Camera (WFPC2) on the Hubble Space Telescope (HST), and spectra taken with the William Herschel Telescope (WHT) and the HST Faint Object Spectrograph (FOS), for the early-type galaxies NGC 4342 and NGC 4570. These galaxies are intermediate between ellipticals and lenticulars, and they both have a small nuclear stellar disc in addition to their main outer disc.

Colour images reveal no colour differences between the nuclear discs and the bulges. Comparison of the  $U - V$  and  $V - I$  colours with stellar population models indicates that the central regions of both galaxies are of intermediate age ( $\sim 8$  Gyr) and of high metallicity. For NGC 4342 this is consistent with the values of the line strengths in the central region derived from the FOS spectra. For NGC 4570, an unusually large  $H\beta$  line strength may suggest recent star formation.

The long-slit WHT spectra have a high signal-to-noise ratio ( $S/N$ ) and a spatial resolution of  $\sim 1''$ . They are used to determine the stellar rotation velocities  $V$ , the velocity dispersions  $\sigma$ , and the deviations of the line-of-sight velocity profiles from a Gaussian shape, as quantified by the Gauss-Hermite moments  $h_3$  and  $h_4$ . Both galaxies are rapidly rotating, and they both have velocity dispersions that increase strongly towards the centre. The  $V$  and  $h_3$  profiles clearly reflect radial changes in the relative contributions of the different structural components identified photometrically.

The FOS was used to obtain spectra with the  $0.26''$  diameter circular aperture at seven different positions in the central region of each galaxy. Measurements of  $V$  and  $\sigma$  yield the stellar kinematics at four times higher spatial resolution than available from the WHT spectra. The FOS spectra of NGC 4342 indicate a central velocity dispersion of  $\sim 420 \text{ km s}^{-1}$ , higher than the  $\sim 320 \text{ km s}^{-1}$  measured from the WHT spectra. Also, the nuclear rotation gradient measured with the FOS is steeper than that measured with the WHT; it reaches  $V_{\text{rot}} \sim 200 \text{ km s}^{-1}$  at  $0.25''$ . The rapid stellar motions seen in the centre of NGC 4342 suggest a large central mass concentration, possibly a massive black hole. The kinematics of the more massive NGC 4570 are less spectacular, with a central velocity dispersion of  $\sim 250 \text{ km s}^{-1}$  and a central rotation curve that reaches only  $\sim 60 \text{ km s}^{-1}$  at  $0.25''$ . The stellar kinematical measurements for both galaxies will be interpreted quantitatively with detailed dynamical models in a series of companion papers.

**Key words:** galaxies: individual: NGC 4342, NGC 4570 – galaxies: elliptical and lenticular, cD – galaxies: nuclei – galaxies: kinematics and dynamics – galaxies: abundances

## 1 INTRODUCTION

The discovery with the Hubble Space Telescope (HST) of a number of early-type galaxies with very small stellar discs, with scale lengths of the order of 20 pc (van den Bosch et al. 1994; Forbes 1994; Lauer et al. 1995), has opened new windows on galaxy dynamics and formation. From a dynamical point of view, nuclear stellar discs are interesting

because their kinematics allow an accurate determination of the central mass density of their host galaxies (van den Bosch & de Zeeuw 1996). The existence of a morphologically and kinematically distinct stellar component in the nucleus of these galaxies raises the question whether they formed coevally with the host galaxy, or arose from evolution of the host galaxy in a later stage. One possible form of evolution would be gas infall to the centre induced by either a bar or a

merger, which after subsequent star-formation could result in a nuclear disc.

Stellar discs with sizes of 0.2–1 kpc were found in several elliptical galaxies from ground-based observations (e.g., Nieto et al. 1991). The nuclear discs discussed here are considerably smaller, and have sizes  $\lesssim 100$  pc. They were discovered in monochromatic broad-band images that were taken with the HST Planetary Camera (PC) before any corrections had been made for the spherical aberration of the HST primary mirror.

To investigate the kinematics of the nuclear discs, and to learn about their formation, we have taken spectroscopic and improved photometric data for two early-type galaxies in the Virgo cluster: NGC 4342 and NGC 4570. These galaxies are intermediate between ellipticals and lenticulars, and in both cases previous HST images revealed the presence of bright nuclear discs (van den Bosch et al. 1994). Global parameters of the two galaxies are listed in Table 1.

We obtained multi-colour ( $U, V, I$ ) images with the second Wide Field and Planetary Camera (WFPC2) aboard the HST, in order to investigate the detailed morphology of the different components in NGC 4342 and NGC 4570, and to study their differences in colour. We also obtained long-slit spectra with the William Herschel Telescope (WHT), and higher spatial-resolution single-aperture spectra with the HST Faint Object Spectrograph (FOS), to determine the stellar kinematics of the different components and investigate the stellar populations. The HST data were obtained after the telescope was serviced to correct for the spherical aberration of the primary mirror.

The nuclear discs have a small angular size, even for HST standards, and are embedded in complex larger structures. Reliable astrophysical interpretation in terms of dynamics and stellar populations therefore requires careful reduction and modeling. In this paper we describe the observations, the reduction, and the parameterization of the results. The quantity and diversity of the data has led us to parameterize it into a form suitable for presentation and modeling. The imaging data is parameterized in terms of both elliptical isophotal parameters and multi-Gaussian decompositions; the kinematic data is parameterized through Gauss-Hermite expansions of the line-of-sight velocity distributions.

A detailed interpretation of the data will be presented in a series of companion papers. Scorza & van den Bosch (1997) will discuss the results of the decomposition of both galaxies into bulge and disc components. Cretton & van den Bosch (1997) will present detailed three-integral modeling of the dynamics of NGC 4342. Van den Bosch & Emsellem (1997) will present evidence that the galaxy NGC 4570 has been shaped under the influence of a rapidly tumbling bar potential.

In Section 2 we present the reduction and parameterization of the multi-colour HST photometry. Sections 3 and 4 contain the reduction of the WHT and HST/FOS spectra, respectively. The stellar kinematical analysis is presented in Section 5. Section 6 discusses the stellar populations of both galaxies, based on the broad-band colour and line strength data. We summarize and discuss our conclusions in Section 7. Throughout this paper we adopt a distance of 15 Mpc for both galaxies, as appropriate for the Virgo cluster (Jacoby, Ciardullo & Ford 1990).

**Table 1.** Parameters of the observed galaxies

NGC	RC2	$M_B$	$D_{25}$ (arcsec)	$V_{\text{hel}}$ (km/s)	$S_{100\mu\text{m}}$ (mJy)	$S_{21\text{cm}}$ (mJy)
4342	S0 <sup>-</sup>	-17.47	84.8	714	$0 \pm 160$	$< 3$
4570	S0	-19.04	244.4	1730	$0 \pm 100$	$< 10$

Column (1) gives the NGC number of the galaxy. Column (2) gives the galaxy type according to the Second Reference Catalogue (RC2; de Vaucouleurs et al. 1976). The absolute blue magnitude (for a Virgo distance of 15 Mpc) is listed in column (3), whereas column (4) gives the major axis isophotal diameter at the surface brightness level  $\mu_B = 25.0$  mag arcsec<sup>-2</sup>. Column (5) lists the heliocentric velocity in km s<sup>-1</sup>. Columns (6) and (7) give upper limits on the IRAS flux density at 100  $\mu\text{m}$  (Knapp et al. 1989) and on the flux density at 21 cm (Wrobel 1991).

**Table 2.** Log of HST/WFPC2 observations

NGC	Filter	colour	date	$t_{\text{exp}}$ (sec)	# exp
4342	F336W	U	21/01/96	3600	4
	F555W	V	21/01/96	200	2
	F814W	I	21/01/96	200	2
4570	F336W	U	19/04/96	5100	5
	F555W	V	19/04/96	400	2
	F814W	I	19/04/96	460	2

Column (4) lists the total exposure time per filter. Column (5) gives the number of exposures per filter.

## 2 HST MULTI-COLOUR PHOTOMETRY

In this section we describe the observations (Section 2.1), the reduction (Section 2.2) and the parameterization of the broad-band WFPC2 images. We derive multi-Gaussian decompositions (Section 2.3) and standard isophotal parameters (Sections 2.4 and 2.5). We also subtract a pure elliptical model from the observations to emphasize the disc structures (Figure 6).

### 2.1 Observations

We obtained  $U$ ,  $V$  and  $I$  band images of NGC 4342 and NGC 4570 using the HST/WFPC2 as part of our GO-project #6107. A detailed description of the WFPC2 can be found in the HST WFPC2 Instrument Handbook (Burrows et al. 1995). The nuclei of the galaxies were centred in the Planetary Camera chip (PC1), which consists of  $800 \times 800$  pixels of  $0.0455'' \times 0.0455''$  each. Exposures were taken with the broad band filters F336W, F555W and F814W; these correspond closely to the Johnson  $U$  and  $V$  bands, and the Cousins  $I$  band, respectively. In each band several separate exposures were taken. Table 2 lists the log of the observations. All exposures were taken with the telescope guiding in fine lock, yielding a nominal pointing stability of  $\sim 3$  mas. Since there was no danger of saturation, the analogue-to-digital gain was set to its low setting of 7.12 electrons/DN (where DN is the number of counts). The CCD read-out noise was 5.24 electrons; the dark rate was only 0.003 electrons pixel<sup>-1</sup>sec<sup>-1</sup>.

## 2.2 Reduction

The images were calibrated with the standard ‘pipeline’ that is maintained by the Space Telescope Science Institute (STScI). The reduction steps, including e.g., bias subtraction, dark current subtraction and flat-fielding, are described in detail by Holtzman et al. (1995a).

Subsequent reduction was done using standard IRAF tasks. With the  $V$ - and  $I$ -band filters, two separate frames were obtained for each galaxy within one HST orbit. These frames were offset from each other by  $11 \times 11$  pixels. This allows removal of chip defects, such as hot pixels and bad columns, as well as cosmic rays. After shifting over an integer  $11 \times 11$  pixels, we checked the alignment of the two frames by measuring the positions of a number of globular clusters present on the PC1. The alignment was found to be better than 0.05 pixels. For the  $U$ -band images, 4-5 separate exposures were available with different exposure times. Frames obtained in different orbits were offset from each other by an integer  $11 \times 11$  pixels. Once again we used globular clusters to determine the offsets, and found them to be accurate at the 0.05-pixel level. Therefore, we could align the frames by shifting over integer pixels, without the need for interpolation. Registered frames for the same galaxy and filter were combined with cosmic-ray rejection. A constant background was subtracted from all combined frames, as measured at the boundaries of the WF2 CCD, where the galactic contribution is negligible.

In order to convert the raw counts in the F336W, F555W and F814W frames to Johnson  $U$  and  $V$ , and Cousins  $I$  band magnitudes, respectively, we performed a flux calibration following the guidelines given by Holtzman et al. (1995b). The equations that convert counts to  $U$ ,  $V$  and  $I$  surface brightness magnitudes include  $U - V$  and  $V - I$  colour terms. We approximated those by the average values found for ellipticals. After the photometric calibration, we calculated the  $U - V$  and  $V - I$  colours from our images, and iterated the calibration until the colours had converged.

For the  $U$ -band, two further corrections are required. First, photometry in the UV is sensitive to the presence of contaminants on the CCD. There is a linear behaviour between the light being lost due to those contaminants and the day since the last decontamination of the CCD. We used the formula of Holtzman et al. (1995b), and applied corrections of 0.0070 and 0.0119 magnitudes to the zero-points of the F336W images of NGC 4342 and NGC 4570, respectively. Secondly, the UV filters have a considerable red leak. Table 6.5 in the WFPC2 Instrument Handbook gives an estimate for the percentage of red light leaking through the filter for a number of stellar spectra. Since early-type galaxies consist mainly of late-type stars, we estimate that 2–15% of the light falling through the F336W filter is coming from wavelengths around 7500Å. We assumed that 8% of the flux through the F336W filter is due to the red leak, and increased the  $U$ -band photometric zero-point by 0.0905 magnitudes. We estimate that our final photometric accuracies are  $\lesssim 0.02$  magnitudes for the  $V$ - and  $I$ -band, and  $\lesssim 0.08$  magnitudes for the  $U$ -band (mainly due to uncertainties in the amount of red leak).

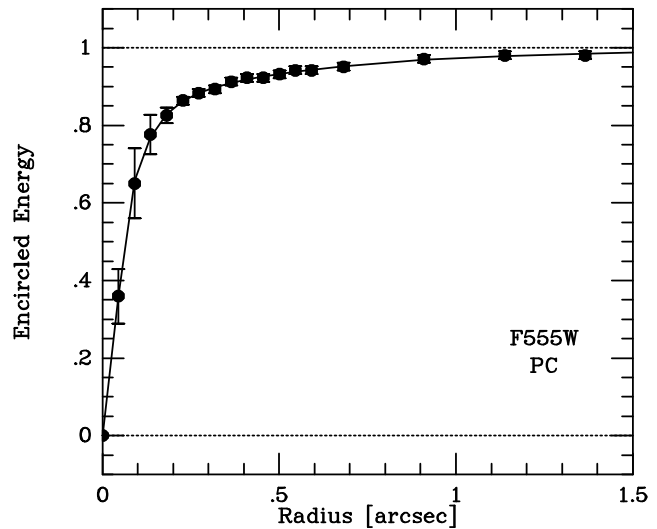


**Figure 1.** The dots show measurements of the encircled energy of the PSF, as a function of radius, for the HST Planetary Camera (PC) with the F555W filter. The solid line is the encircled energy of the model PSF used in the MGE method. This is a sum of 5 circular Gaussians.

## 2.3 Multi-Gaussian fitting

The HST point-spread-function (PSF) has improved significantly with the 1993 refurbishment mission. Figure 1 shows measurements of the encircled energy curve for the F555W filter and the PC CCD (Holtzman et al. 1994). The FWHM of the PSF is only  $\sim 0.1''$ . However, the PSF wings are still very broad; several percent of the light is scattered more than 1 arcsec away. Since the luminosity profiles of NGC 4342 and NGC 4570 are strongly peaked towards the centre, PSF convolution still has a considerable degrading effect. Deconvolution therefore remains essential to obtain the maximum amount of information from our images. We have explored two methods of PSF deconvolution: the Multi Gaussian Expansion (MGE) method (this section), and direct Richardson-Lucy deconvolution (Section 2.4).

The MGE method was developed by Monnet, Bacon & Emsellem (1992). It builds a model for the galaxy, while deconvolving for the effects of PSF convolution at the same time. The method assumes that both the PSF and the deconvolved (i.e., intrinsic) surface brightness distribution of the galaxy can be approximated by a sum of Gaussians. Each Gaussian is parameterized by 6 parameters: the centre  $(x_i, y_i)$ , the position angle, the flattening  $q_i$ , the standard deviation  $\sigma_i$ , and the central intensity  $I_i$ . We approximated the HST  $V$ -band PSF as the sum of 5 circular (i.e.,  $q = 1$ ) Gaussians, chosen so as to fit the observed encircled energy curve (Figure 1). Using this PSF model we derived the parameters of the  $N$  Gaussians that describe the *deconvolved* surface brightness, by fitting to the HST  $V$ -band galaxy images. Since both the PSF and the deconvolved surface brightness are assumed to be sums of Gaussians, the convolution is analytical. In the fitting we forced each of the  $N$  Gaussians to have the same position angle and centre (i.e., the MGE model is assumed to be axisymmetric). Therefore, the model is described by  $3N + 3$  free parameters, which are fit simultaneously to the images using a global

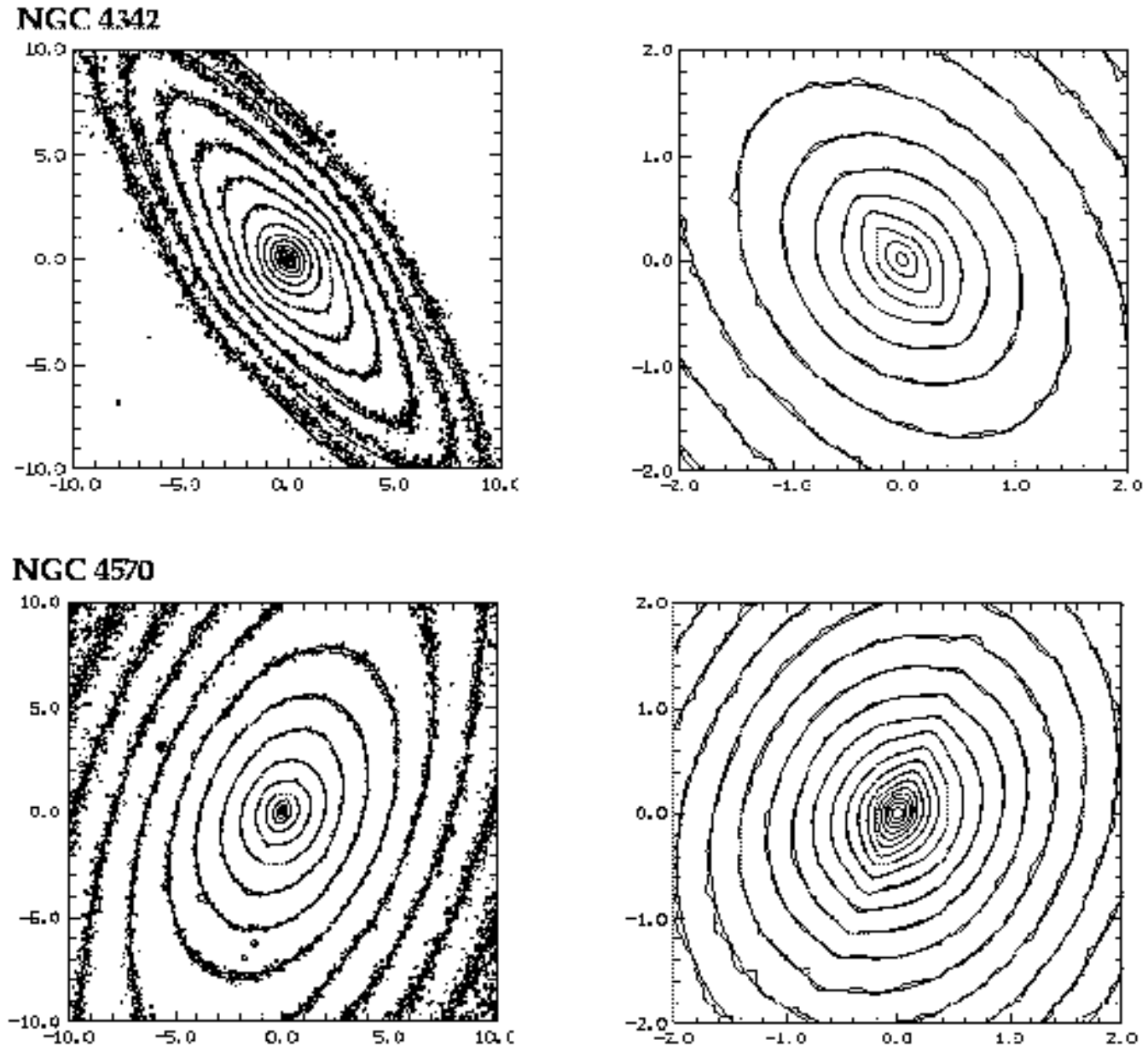


**Figure 2.** Contour maps of the WFPC2 *V*-Band images of NGC 4342 and NGC 4570 (without PSF deconvolution), at two different scales:  $20'' \times 20''$  (plots on the left) and  $4'' \times 4''$  (plots on the right). Contours of the best-fitting MGE models are superimposed.

bidimensional fitting process. More and more components are added until convergence is achieved (for details on the MGE method, see Emsellem, Monnet & Bacon, 1994). We found our fits to converge for  $N = 11$  Gaussian components, for both NGC 4342 and NGC 4570.

The results are shown in Figure 2, which displays contour maps of the HST *V*-band images, with superimposed the best fitting MGE-models. In general the fits are excellent. For NGC 4342 a small discrepancy is seen on the outside. This is due to the fact that the isophotes of this galaxy twist slightly at large radii (see Section 2.5), which we ignore by forcing the position angles of the different Gaussians to be the same. In both galaxies there is a clear multi-component structure: the isophotes are highly flattened and discy at the outside (due to the outer disc), less flattened at

intermediate radii ( $r \approx 1''$ ), where the bulge is dominating the light, and again very elongated and discy close to the centre, due to the nuclear disc. The parameters of the MGE models are listed in Table 3.

## 2.4 Luminosity profiles

Richardson-Lucy iteration (Lucy 1974) provides an alternative PSF deconvolution method. For this, accurate knowledge of the PSF is required. We calculated model PSFs appropriate for each given filter and position of the nucleus on the PC1 CCD, using the TinyTim software package. Since our observations were made while guiding in fine lock, no corrections for telescope jitter were necessary.

We used the Richardson-Lucy algorithm to deconvolve

**Table 3.** Parameters of MGE models for the deconvolved  $V$ -band surface brightness

$i$	NGC 4342			NGC 4570		
	$I_i$ ( $L_{\odot}\text{pc}^{-2}$ )	$\sigma_i$ (arcsec)	$q_i$	$I_i$ ( $L_{\odot}\text{pc}^{-2}$ )	$\sigma_i$ (arcsec)	$q_i$
1	3136240.0	0.02	0.119	1755160.0	0.02	0.158
2	95319.8	0.08	0.841	61238.0	0.09	0.800
3	42954.3	0.26	0.632	21526.4	0.23	0.748
4	48520.9	0.36	0.136	21589.3	0.26	0.140
5	17155.4	0.42	0.848	11285.3	0.51	0.780
6	4930.9	0.72	0.521	5728.7	0.60	0.120
7	8657.3	0.79	0.840	7911.9	1.11	0.809
8	3207.9	1.80	0.759	3800.5	2.73	0.635
9	2154.3	3.89	0.275	1624.8	4.20	0.700
10	1085.9	9.11	0.270	1095.8	12.88	0.350
11	219.1	9.61	0.836	334.4	17.12	0.583

Column (1) gives the index number of each Gaussian. Columns (2) and (5) give its central surface brightness, columns (3) and (6) give its standard deviation, and columns (4) and (7) give its flattening.

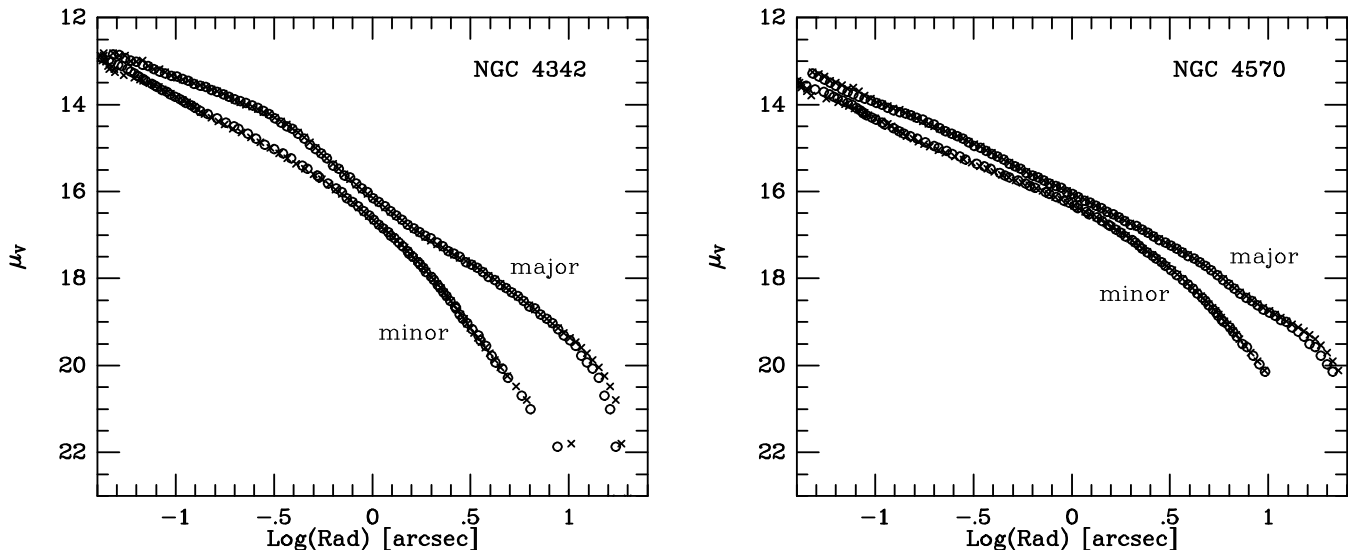


**Figure 3.** The projected  $V$ -band surface brightness profiles (in  $\text{mag arcsec}^{-2}$ ) of the Lucy-deconvolved (open circles) and MGE-deconvolved (crosses) images of NGC 4342 and NGC 4570. Agreement between the two methods of deconvolution is excellent. Profiles along both the major and the minor axes are shown. The excess light along the major axes clearly reveals the ‘double-disc’ structure in both galaxies. The minor axis profiles show that the bulges have a luminosity profile similar to that of low-luminosity elliptical galaxies, with very steep cusps.

the  $V$ -band images of NGC 4342 and NGC 4570; 20 iterations were found to be sufficient for convergence. We subsequently derived the luminosity profiles along the major and minor axes, using the isophote fitting procedure described below (Section 2.5). The resulting  $V$ -band surface brightness profiles are shown in Figure 3 (open circles). The difference between the major and minor axis profiles clearly reveals the excess light due to the nuclear and outer disc components. The minor axis profiles, which have a negligible contribution of disc light, show a double power-law behaviour for the bulge luminosity distribution, with a steep cusp. Such profiles are characteristic for low luminosity ellipticals (Gebhardt et al. 1996). The bulge luminosity profiles will be further discussed by Scorza & van den Bosch (1997).

The crosses in Figure 3 correspond to the same luminosity profiles but now determined from the MGE model of the

intrinsic (i.e., deconvolved) surface brightness, again using the isophote-fitting procedure. The agreement with the luminosity profiles derived from the Lucy-deconvolved images is excellent. Small discrepancies can be seen at the outside. These are related to the discrepancies seen in Figure 2 and originate from neglecting the small amount of isophote twisting, when constructing the MGE models.

## 2.5 Isophotal analysis

We derived the ellipticity and position angle of the isophotes, as a function of radius, for each colour and each galaxy, from the non-deconvolved images. In addition, the  $\sin 3\theta$  and  $4\theta$  terms were derived that describe the high-order deviations of the isophotes from pure ellipses (e.g., Lauer 1985; Jedrzejewski 1987; Bender, Döbereiner & Möllenhoff

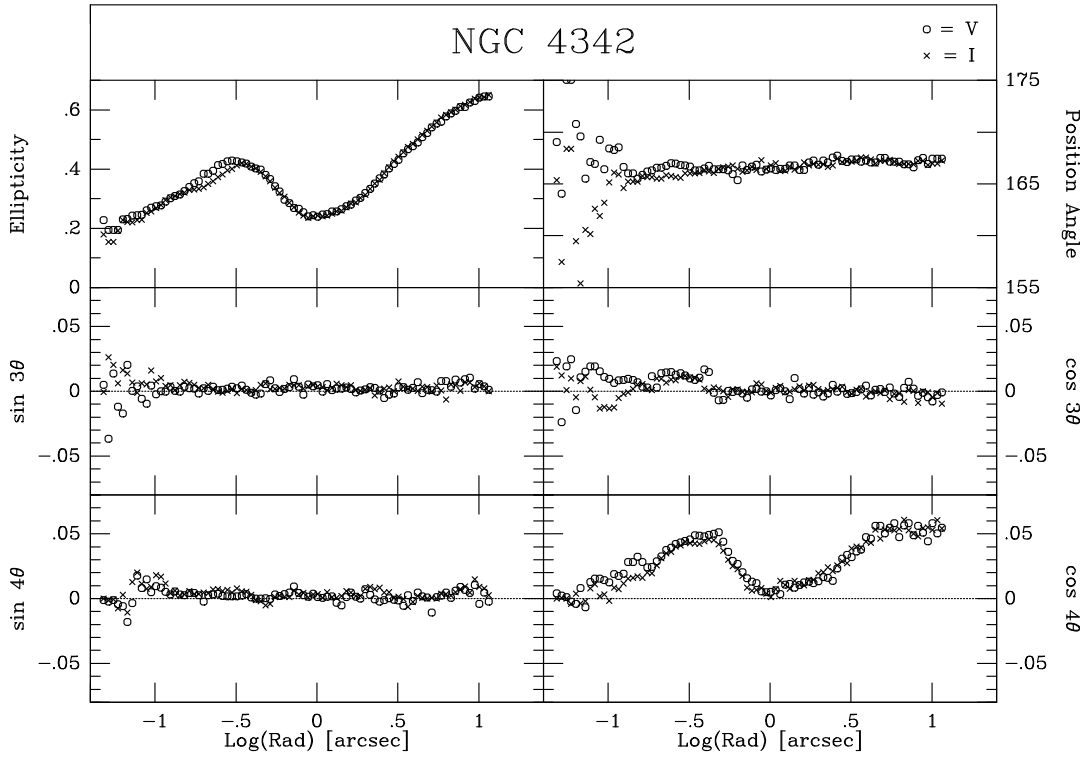


**Figure 4.** The isophotal parameters as a function of  $\log(\text{radius})$ , for the V- and I-band images of NGC 4342. Both the ellipticity and the  $\cos 4\theta$ -term clearly reveal the double-disc structure.

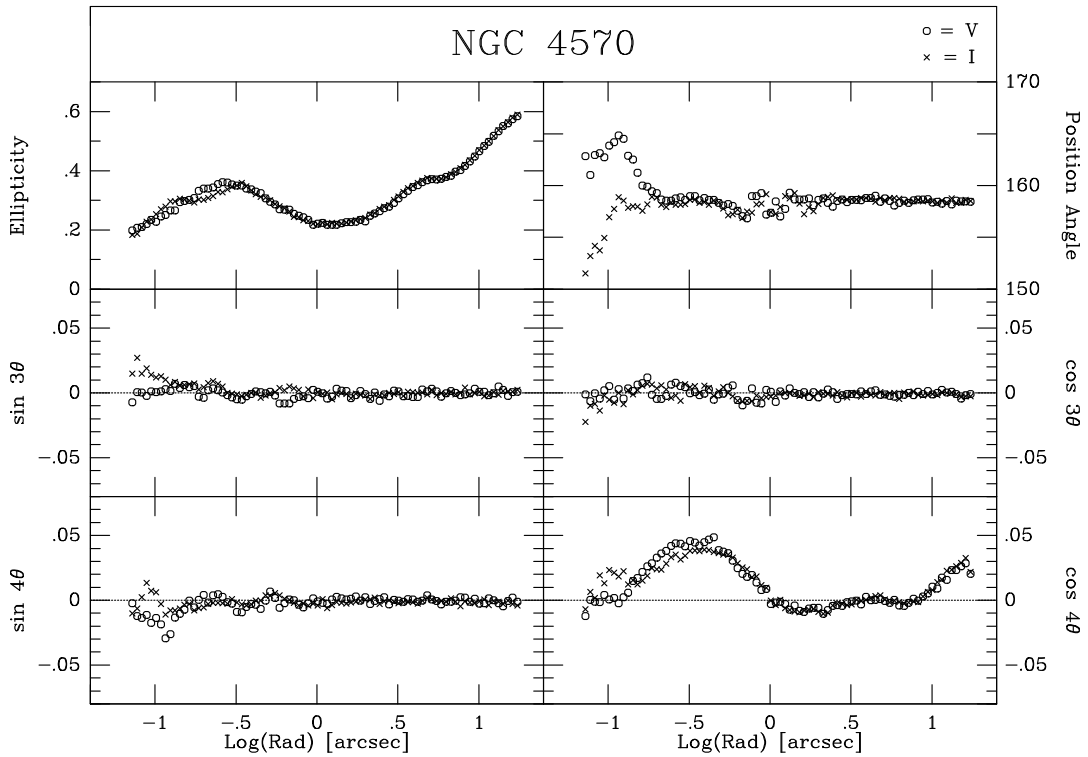


**Figure 5.** Same as Figure 4, but now for NGC 4570.

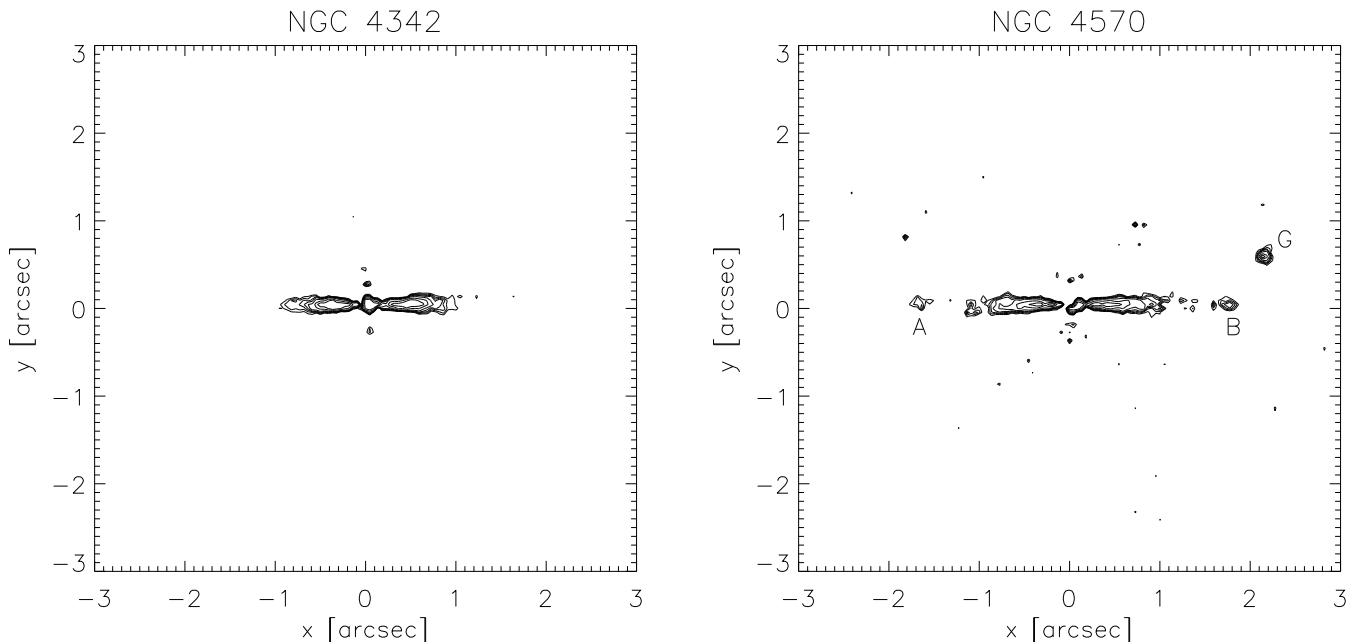


**Figure 6.** Contour maps of the  $V$ -band residual images of NGC 4342 (left) and NGC 4570 (right), obtained after subtraction of perfectly elliptical galaxy models. The images were rotated to align the major axis of each galaxy with the  $x$ -axis. Highly flattened nuclear discs are clearly visible inside the central arcsec. Only positive contours are plotted for clarity. The apparent central point sources are artifacts, due to the limited radial extent of the galaxy models that were subtracted. The features ‘A’ and ‘B’ in NGC 4570 are both at  $1.7''$  from the centre, and will be discussed elsewhere. The feature marked ‘G’ is a globular cluster.

1988). For a pure ellipse, these coefficients are all equal to zero. Positive  $\cos 4\theta$  terms correspond to ‘discy’ isophotes, whereas ‘boxy’ isophotes give rise to negative values of the  $\cos 4\theta$  term.

The results for the  $V$ - and  $I$ -band images are shown in Figures 4 and 5. Again, the double-disk structure of both galaxies is clear: the isophotes are highly flattened and discy at the outside ( $r > 1''$ ), moderately flattened and nicely elliptical at intermediate radii ( $r \approx 1''$ ), and again strongly elongated and discy inside  $1''$ . At radii inside  $\sim 0.5''$ , the measured parameters are not a reliable representation of their intrinsic values, due to the convolution with the HST PSF.

For both galaxies, there is almost no difference between the  $V$ - and  $I$ -band parameters. The same appears to be true for the  $U$ -band parameters (not plotted here), although these are noisier due to lower  $S/N$ . Except for the  $\cos 4\theta$  term, all other high-order terms that express deviations from elliptical isophotes are close to zero. For both galaxies the position angle is close to constant, although in NGC 4342 there is a mild, but significant twist of a few degrees. Comparison with the isophotal parameters derived from Lucy deconvolved F555W images obtained with the PC before the HST refurbishment (van den Bosch et al. 1994) generally shows good agreement, with one exception. The pre-refurbishment images revealed strange ‘wiggles’ in the higher order terms of the Fourier expansion, interpreted by van den Bosch et al. (1994) as indicative of a patchy dust distribution. However, from the WFPC2 images presented here no such evidence for dust is found. It therefore seems likely that the pre-refurbishment images suffered from insufficiently corrected measles due to contaminants.

Michard (1994) showed that the inner isophotes of strongly flattened galaxies containing a sharp central feature are distorted in the process of convolution and subsequent deconvolution, in a way that can mimic the presence of a nuclear disc. Michard therefore suggested that the nuclear discs inferred from isophotal analysis of deconvolved images could be merely an artifact of the deconvolution procedure. Van den Bosch et al. (1994) found similar deconvolution induced distortions from tests performed on model galaxies and concluded that the isophotal parameters inside  $0.5''$  (e.g., five times the FWHM of the PSF) indeed could not be trusted. Their evidence for the presence of nuclear discs was therefore based solely on the photometry outside  $0.5''$ . The new data presented here clearly shows the nuclear discs in NGC 4342 and NGC 4570 even in data that are *not* deconvolved (Figures 2, 4 and 5). This proves incontrovertibly that the nuclear discs are real structures.

In order to reveal more clearly the nuclear discs, we constructed residual  $V$ -band images by subtracting a model image that has the same luminosity and ellipticity profile as the real image, but is taken to have perfectly elliptical isophotes. These residual images reveal the structures that are responsible for the higher-order deviations from perfectly elliptical isophotes. Contour maps of these images are shown in Figure 6. We only show the inner  $3'' \times 3''$  regions where the nuclear discs clearly stand out. The models that were subtracted from the images are based on the isophotal parameters outside  $0.1''$ ; inside that radius no meaningful isophotes can be fitted. As a resulting artifact, the residual images show a central point source in addition to the nuclear discs. The residual image of NGC 4570 reveals, besides the nuclear disc, two unresolved features, marked ‘A’ and ‘B’.

These features are both at  $1.7''$  offset from the centre, and are perfectly aligned with the nuclear disc. The nature of these features is discussed in van den Bosch & Emsellem (1997). The feature marked ‘G’ is a globular cluster.

### 3 GROUND-BASED SPECTRA

We obtained high- $S/N$ , ground-based, long-slit spectra of NGC 4342 and NGC 4570, with a spatial resolution of  $\sim 1''$ , using the 4.2m WHT on La Palma. In this section we describe the observations (Section 3.1), the reduction (Section 3.2), the seeing PSF of the observations (Section 3.3), and our observations of a library of template stars for use in the kinematical analysis (Section 3.4).

#### 3.1 Observations

The observations were done in March 1994 with the WHT/ISIS spectrograph. With ISIS two spectra are obtained simultaneously, on the red and blue arms of the spectrograph. On both arms we used the high resolution gratings with 1200 lines/mm. The red arm was centred around the Ca II triplet (8498, 8542, 8662Å), while the blue arm covered the Mg *b* triplet (5167, 5173, 5184Å). The blue spectra were irreparably disturbed by an internal reflection (‘ghost’) and will not be further discussed.

On the red arm we used a Tek CCD of  $1124 \times 1124$  pixels. Each pixel measures  $0.36''$  by  $0.41\text{Å}$ . All spectra were obtained with a slit width of  $1''$ , which is roughly equal to the average seeing. The instrumental resolution, expressed as the Gaussian dispersion of spectral lines in the arc lamp frames, was  $9\text{ km s}^{-1}$ .

The galaxy exposures were split into consecutive exposures of typically 20-30 minutes. Before each galaxy exposure we took exposures of arc lamps to allow accurate wavelength calibration. Bias frames, tungsten lamp flats and sky flats were taken during twilight. We also took spectra of a spectro-photometric standard, to allow correction for the wavelength sensitivity of the CCD (see Section 3.2). A log of the galaxy observations is given in Table 4.

Guiding during each exposure was done with a TV camera with a Johnson *V*-band filter. Differential atmospheric refraction can play an important role, because the *V*-band central wavelength ( $\lambda_{\text{cen}} = 5500\text{Å}$ ) is offset considerably from the central wavelength of our red spectra ( $\lambda_{\text{cen}} = 8580\text{Å}$ ). This results in an offset of the slit from the intended position on the galaxy that was selected with the TV camera. These offsets can be calculated and are listed in Table 4. Note that for the ‘offset exposure’ of NGC 4570 we aimed for an intentional offset of  $1.5''$ , perpendicular to the major axis. However, due to the atmospheric refraction the real offset only amounted to  $0.94''$ . Differences in atmospheric refraction over the observed spectral range (8390–8770Å) are at most  $0.03''$ , and can be neglected.

#### 3.2 Reduction

All spectra were reduced using IRAF. The bias level was determined from the overscan columns and subtracted. For each night two flat-field frames were created. The tungsten flats were used to create one high- $S/N$  flat-field that shows the pixel-to-pixel sensitivity variations of the CCD.

**Table 4.** Log of long-slit WHT observations

NGC	slit pos.	PA	slit ( $''$ )	$S$ ( $''$ )	exp (min)	airmass	off ( $''$ )
4342	major axis	347	1.0	0.80	90	1.10	0.15
	minor axis	257	1.0	0.95	90	1.52	0.24
4570	major axis	159	1.0	1.10	80	1.12	-0.22
	offset axis	159	1.0	1.05	70	1.38	0.94
	minor axis	249	1.0	1.70	60	1.19	0.17

Column (3) gives the position angle of the slit in degrees. The slit width is given in column (4). Column (5) gives the seeing FWHM  $S$ , defined as in Section 3.3. The exposure time is given in column (6), and the airmass during each exposure in column (7). Column (8) gives the offset of the slit from the centre, corrected for differential atmospheric refraction.

The spectra of the twilight sky were used to construct a high- $S/N$  flat-field that shows the large scale illumination pattern due to vignetting of the slit. Both flat-fields were normalized and divided into all spectra.

Cosmic rays were removed from all frames by interpolating over high- $\sigma$  deviations, as judged from Poisson statistics and the known gain and read-out noise of the detector. The wavelength calibration was done using the arc-lamp frames. Spectra were rebinned using the resulting wavelength solution, both in the spatial direction (to align the direction of dispersion with the rows of the frames), and in logarithmic wavelength. The latter was done to a scale of  $11.076\text{ km s}^{-1}/\text{pixel}$ , covering the wavelength range from 8390Å to 8770Å. Subsequently, we determined the sensitivity as a function of wavelength from the spectra of the spectro-photometric standards, and corrected all spectra for these sensitivity variations. All exposures of the same galaxy and slit position were added. Sky spectra were determined from the data beyond  $90''$  from the centre of the slit, and were subtracted. Template star frames (see Section 3.4), were summed along columns to yield one high- $S/N$  spectrum for each star.

#### 3.3 Seeing estimates

*I*-band images of photometric standard fields were taken during the observing run using the Cassegrain focus Auxiliary Port of the WHT. The detector used was a EEV CCD with  $0.10'' \times 0.10''$  pixels. The images were bias subtracted, flat-fielded, and cleaned of cosmic rays.

The shape of the seeing PSF was determined using bright stars on these images. For all images obtained throughout the run, the shape could be well described by a sum of two Gaussians:

$$\text{PSF}(r) = A_1 e^{-r^2/2\sigma_1^2} + A_2 e^{-r^2/2\sigma_2^2}, \quad (1)$$

with fixed ratios of the dispersions,  $\sigma_2/\sigma_1 = 1.65$ , and amplitudes,  $A_2/A_1 = 0.22$ , of the two components. The PSF is normalized for  $A_1 = 0.09897/\sigma_1^2$ , and is fully specified by its FWHM  $S = 2.543\sigma_1$ .

The auto-guider camera provides an independent measure of the seeing FWHM,  $S_{\text{auto}}$ , during each exposure. However, this measure does not necessarily take the full PSF shape (equation 1) into account. In addition, the auto-guider was equipped with a *V*-band filter, whereas our Ca II triplet spectra fall in the *I*-band. We therefore calibrated the autoguider FWHM estimates, by comparing them to



**Table 5.** HST/FOS observations: log and kinematical results

id.	Galaxy	$x_{\text{ap}}$ (arcsec)	$y_{\text{ap}}$ (arcsec)	$t_{\text{exp}}$ (sec)	Intensity (counts/sec)	$\gamma$	$\Delta\gamma$	$V_{\text{rot}}$ (km s <sup>-1</sup> )	$\Delta V$ (km s <sup>-1</sup> )	$\sigma$ (km s <sup>-1</sup> )	$\Delta\sigma$ (km s <sup>-1</sup> )
A1	NGC 4342	-0.014	-0.010	1000	1421.1	1.132	0.079	-0.2	30.8	418.3	32.7
A2		+0.236	-0.010	1190	746.3	1.165	0.091	+188.2	25.5	321.1	33.3
A3		-0.264	-0.010	1200	714.4	1.281	0.089	-202.1	21.1	308.2	26.8
A4		+0.486	-0.010	990	407.6	1.025	0.174	+239.8	55.0	312.7	53.5
A5		-0.514	-0.010	900	384.3	1.285	0.152	-253.7	25.1	237.5*	23.9
A6		+0.098	+0.214	500	456.6	1.447	0.185	+111.0	49.0	327.2	50.2
A7		-0.126	-0.234	570	521.4	1.152	0.177	-185.2	73.0	391.9	101.0
B1	NGC 4570	-0.011	-0.052	810	866.5	1.147	0.082	+35.8	25.0	249.4	31.9
B2		+0.239	-0.052	450	434.9	1.335	0.158	-4.1	31.7	217.6	38.0
B3		-0.261	-0.052	450	446.6	1.323	0.162	-119.7	41.0	205.8	38.9
B4		+0.489	-0.052	450	273.7	0.990	0.168	+104.2	27.7	121.7	46.9
B5		-0.511	-0.052	450	267.3	1.073	0.159	-108.9	39.9	170.8*	20.6
B6		-0.011	+0.198	450	360.8	1.279	0.162	+79.3	34.2	183.3	41.5
B7		-0.011	-0.302	450	306.3	1.466	0.230	+102.4	78.5	332.9	78.2

Column (1) gives the label for the spectrum used in the remainder of the paper. Columns (3) and (4) give the aperture position in a  $(x, y)$  coordinate system centred on the galaxy, and with  $x$  along the major axis. Column (5) gives the exposure time. In Column (6) we list the observed intensity, integrated over the wavelength range covered by the grating. Columns (7)–(12) give the results of the kinematical analysis and their errors;  $\gamma$  is the line strength,  $V_{\text{rot}}$  the rotation velocity, and  $\sigma$  the velocity dispersion. Asterisks indicate dispersions that were used as reference dispersions (see Appendix A).

the FWHM values,  $S_{\text{image}}$ , inferred from double-Gaussian fits to the images of bright stars on the  $I$ -band Auxiliary Port exposures. This yielded  $S_{\text{image}}/S_{\text{auto}} \approx 1.0$ , indicating that  $S_{\text{auto}}$  can be used directly as an estimate of the true  $I$ -band seeing FWHM. The FWHM values  $S$  in Table 4 list the seeing FWHM thus obtained for each of our spectra.

As a consistency check, we convolved the Lucy-deconvolved  $I$ -band HST image of NGC 4342 with the PSF of equation (1), for different test values of the FWHM  $S$ . We subsequently overlaid a slit (with the same width and position angle as for the WHT spectra), and binned into pixels of the appropriate size. This profile was then compared to the observed intensity profile along the slit for each of the spectra. In all cases we found the best-fitting values of  $S$  to be consistent with the FWHM values listed in Table 4.

### 3.4 Template spectra

To infer stellar kinematical quantities from the galaxy spectra, they must be compared to a template spectrum. It is important to choose a template that closely matches the ‘average’ spectrum of the stars in the galaxy (without kinematical Doppler broadening), to minimize possible systematic errors (e.g., van der Marel et al. 1994). Most of the visible light of elliptical galaxies comes from stars on the giant, asymptotic, and horizontal branches, and their spectra are therefore comparable to those of G and K giants. The spectrum of a single K giant star generally makes a reasonable template, but not an ideal one, because galaxies are made up of stars of different stellar types. We therefore observed 13 template stars with spectral types ranging from F7 to M0. All these spectra were taken with the same instrumental setup as the galaxy spectra, and were reduced in the same way. We used this template library to determine the mix of template stars that best matches the galaxy spectra. We assume that there are no strong changes in stellar population over the galaxy, and we therefore determined only one

optimal template spectrum per galaxy. For this purpose we summed the spectra along the major axes of NGC 4342 and NGC 4570 inside the inner  $1''$ , to yield one high- $S/N$  spectrum per galaxy. We then used a method similar to a ‘biased random walk’, in order to search for the optimal template that consists of a weighted sum of the stellar spectra in the library (van der Marel 1994).

## 4 HST SPECTRA

In this section we discuss the high spatial resolution spectra obtained with the HST/FOS. We describe the observations (Section 4.1), the target acquisition (Section 4.2), the reduction (Section 4.3), the wavelength calibration (Section 4.4), and our choice of template spectrum for use in the kinematical analysis (Section 4.5). A detailed description of the FOS can be found in the HST/FOS Instrument Handbook (Keyes et al. 1995).

### 4.1 Observations

We obtained spectra of NGC 4342 and NGC 4570 with the HST/FOS, using the circular  $0.26''$  diameter aperture (the so-called FOS 0.3 aperture) and the G570H grating. This grating covers the wavelength range from 4569 to 6818Å, and has a dispersion of 4.37Å per diode. The main absorption lines in this spectral range are the Mg  $b$  triplet (5167, 5173, 5184Å) and the Na D lines at 5892Å. The spectra were quarter-stepped, yielding 2064 1/4-diode pixels of 1.09Å. For each galaxy, 7 spectra were taken at different aperture positions, as illustrated in Figure 7 and summarized in Table 5.

### 4.2 Target acquisition

Some form of target acquisition is required to properly position the galaxy in the  $0.26''$  aperture. We used the ‘peak-up’ acquisition mode to centre the aperture on the nucleus

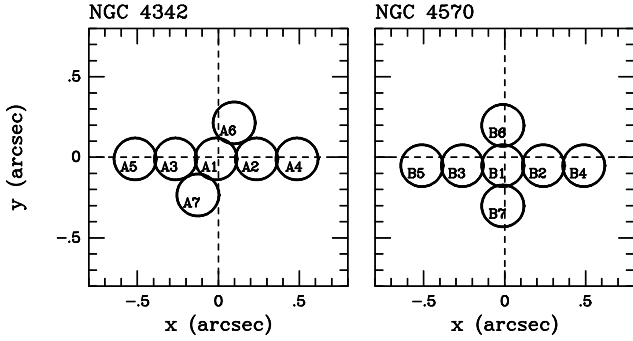


**Figure 7.** Aperture positionings for the HST/FOS spectra. The labels are as in Table 5.

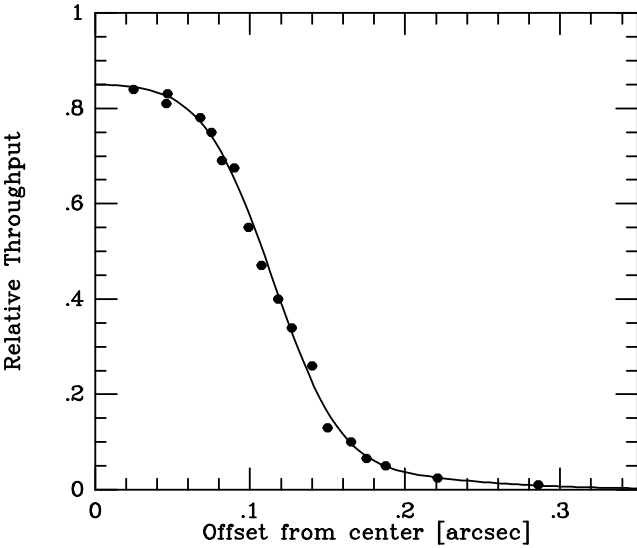


**Figure 8.** The aperture transmission for a star in the circular  $0.26''$  aperture (nominal size), as a function of its distance from the aperture centre. Data points are from Evans (1995). The relative throughput is normalized to 1.0 for a star centred in the circular  $0.86''$  diameter aperture (the FOS  $1.0$  aperture). The solid line is our model fit, which assumes a PSF that is a sum of three circularly symmetric Gaussians, and an aperture diameter of  $0.238''$ .

of each galaxy; spectra at offset positions were obtained by slewing the telescope from this position. Pointing drifts during the observations are generally not significant ( $\lesssim 0.03''$ ; Keyes et al. 1995). The acquisition consists of different stages. In each stage the total flux through an aperture is measured for a grid of aperture positions. The telescope is then centred on the aperture position with the highest flux. In each subsequent stage a smaller aperture is used with a tighter grid (smaller inter-point spacings), thus increasing the accuracy of the target positioning. We used different target acquisition patterns for NGC 4342 and NGC 4570. For NGC 4570, the final stage consisted of a  $3 \times 3$  grid with  $0.1''$  inter-point spacings, using the circular  $0.26''$  aperture. This yields an expected pointing accuracy  $\lesssim 0.08''$  (Keyes et al. 1995). For NGC 4342, a  $5 \times 5$  grid with  $0.052''$  inter-point spacings was adopted, again using the  $0.26''$  aperture, yielding an expected pointing accuracy  $\lesssim 0.04''$ .

Precise knowledge of the aperture positions is of great importance when interpreting the data and comparing it

to models. We therefore modeled the observed fluxes in the final peak-up stage to verify the success of the target acquisition. We denote the offset of the true galaxy centre from the grid position that produced the most counts in the final peak-up stage by  $(\Delta_x, \Delta_y)$ . Here  $x$  is along the major axis of the galaxy. We adopt the MGE-model for the V-band WFPC2 data to describe the intrinsic surface brightness distribution of each galaxy. For a given offset  $(\Delta_x, \Delta_y)$ , one may calculate the predicted flux at each grid point in the final peak-up stage, taking into account the HST/FOS PSF and the aperture size. These predictions can be compared to the observed fluxes, and the best-fitting offset  $(\Delta_x, \Delta_y)$  can be determined using  $\chi^2$ -minimization. The result describes the accuracy of the target acquisition.

To properly model the observations one must know the spatial convolution kernel due to the combined effects of the HST/PSF and the aperture size, neither of which has been particularly well calibrated previously. We therefore performed a new calibration of these quantities, using existing observations obtained by Evans (1995). This follows the approach of van der Marel et al. (1997), who did the same for the small *square* FOS apertures. Evans measured the throughput of the  $0.26''$  diameter for a star positioned at various distances from the aperture centre, as shown in Figure 8. We fitted these data under the assumption of a purely circular aperture, and a PSF that can be described as the sum of circularly symmetric Gaussians. No good fit could be obtained if the aperture diameter was kept fixed at its nominal value of  $0.26''$ . This can be due either to the fact that our model ignores the effects of diffraction at the aperture edges, or because the aperture does in fact have a different diameter than its nominal value. An excellent fit to the calibration observations could in fact be obtained (solid curve in Figure 8) if the aperture diameter was treated as a free parameter, yielding a value of  $0.238''$ . The solid curve in Figure 8 shows the fit under the assumption that the PSF can be described by the sum of three Gaussians. The question whether the true aperture diameter is  $0.26''$  or  $0.238''$  is not relevant here; the diameter enters into the analysis only through the kernel that describes the combined effect of the PSF and the aperture size. This kernel is adequately fit by our model, independent of what the actual aperture size is.

The peak-up data for the final stage of the NGC 4342 target acquisition are shown in Figure 9. It displays the count rate measured at each of the 25 positions in the  $5 \times 5$  grid at which the  $0.26''$  aperture was placed. The curve shows the predictions of our best-fit model, which provides an excellent fit. It has an offset  $(\Delta_x, \Delta_y)$  of only  $(+0.014'', +0.010'')$ . Similar models for the NGC 4570 data indicate a somewhat larger offset of  $(+0.011'', +0.052'')$ . From a number of experiments we estimate the errors on our determination of  $\Delta_x$  and  $\Delta_y$  to be smaller than  $0.005''$ . Thus the peak-up acquisitions worked well for both galaxies, and our models yield the precise positions of the apertures to high accuracy.

### 4.3 Reduction

The spectra were reduced using the standard pipeline procedure described by Keyes et al. (1995). The pipeline flat-field was checked by cross-correlating it with our continuum subtracted galaxy spectra. A clear cross-correlation peak

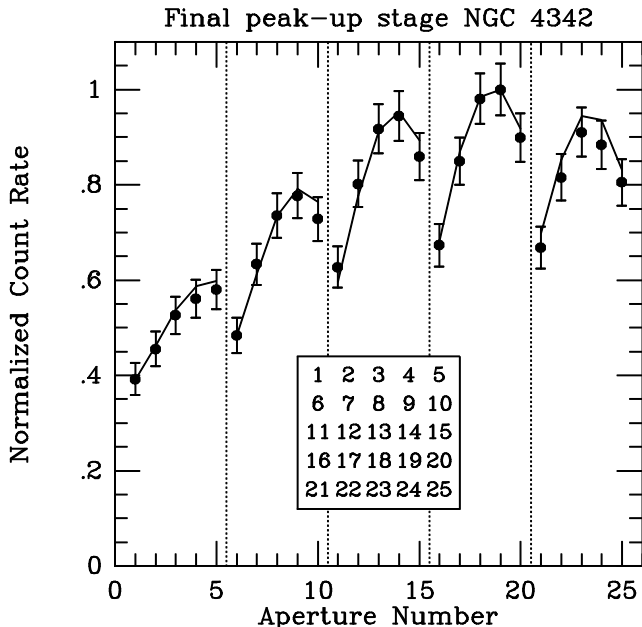


**Figure 9.** Results of the final peak-up stage on the nucleus of NGC 4342. The  $0.26''$  aperture was placed at the positions of a  $5 \times 5$  grid on the sky, as illustrated in the inset. The data points show the measured counts for each aperture position, normalized to unity for the position with the maximum count rate (position #19). The error bars indicate the Poisson noise on the measurements. The solid curves connect the predictions of the best-fit model for these data. This model is based on convolutions of the WFPC2 *V*-band image, and assumes that the centre of NGC 4342 is offset from the centre of aperture position #19 by  $-0.014''$  along the major axis, and  $-0.010''$  along the minor axis.

at zero shift confirmed the appropriateness of the flat-field. The spectra were converted from counts to  $\text{erg cm}^{-2} \text{s}^{-1} \text{\AA}^{-1}$  using the inverse sensitivity file (IVS) for the circular  $0.26''$  aperture. We did not attempt to correct the calibrated spectra for the PSF dependence on wavelength; this only affects the continuum slope, which is subtracted in the stellar kinematical analysis anyway.

#### 4.4 Wavelength calibration

A vacuum wavelength scale is computed by the STScI pipeline, based upon dispersion coefficients for the given grating and aperture. Due to non-repeatability of the filter-grating wheel and the aperture wheel, offset errors in the wavelength scale can occur of up to several Angstroms. Since we changed neither the aperture nor the grating during our visits, this will not affect the relative velocity scale for each galaxy. It may affect the absolute velocity scale, but that is of little importance.

The FOS suffers from the so-called ‘geomagnetically induced image motion problem’ (GIMP). Although on-board corrections are applied to correct for this, residual effects still affect the wavelength scale considerably ( $0.13\text{\AA}$  RMS, according to the HST Data Handbook). Additional wavelength calibration is therefore useful. For NGC 4570, one arc lamp spectrum was obtained after the acquisition. We used this spectrum to check the pipeline wavelength calibration, by comparing the wavelengths of the emission line centres

to their actual vacuum wavelengths. In addition to an offset of  $\sim 2\text{\AA}$  (due to the non-repeatability of the wheels), a small non-linearity of the wavelength scale was found. We therefore recalibrated the wavelength scale using the arc spectrum, including an additional shift of  $-0.769\text{\AA}$  to correct for the offset between internal and external sources (Keyes et al. 1995). For NGC 4342, an arc lamp spectrum was obtained at the end of each orbit. The wavelength scale of these spectra was found to vary by  $0.35\text{\AA}$  during the visit, as a result of residual GIMP. The arc spectra were used to recalibrate the wavelength scale of each galaxy spectrum. For this, we used linear interpolation in time to estimate the wavelength scale for observations between two arc spectra. After wavelength recalibration, all spectra were rebinned logarithmically to a scale of  $58.539 \text{ km s}^{-1}/\text{pixel}$ , covering the wavelength range between  $4570$  and  $6817\text{\AA}$ .

We estimate the uncertainties in the final wavelength scale for NGC 4342 to be  $\lesssim 3.5 \text{ km s}^{-1}$ . For NGC 4570, we could not correct for residual GIMP variations from orbit to orbit, because only one arc lamp spectrum was obtained. If the variations of the absolute wavelength scale were of the same order as during the NGC 4342 visit (i.e.,  $0.35\text{\AA}$ ), the absolute velocity scales of different NGC 4570 spectra may vary by  $\sim 20 \text{ km s}^{-1}$ . This may induce systematic errors in the rotation velocities of the same order (see Section 5.2).

#### 4.5 Template spectra

To facilitate the kinematical analysis it is convenient to have template spectra that are observed with the same instrumental setup. However, because of the time consuming target acquisitions, only very few template stars have been observed with the FOS. From the HST archive we took a spectrum of the KIII-star F193, which was observed with the same setup as our galaxy spectra under GO proposal 5744 (PI: H.C. Ford). Unfortunately, after reducing the spectrum, it was found to provide a poor match to our galaxy spectra.

We therefore decided to use a template library obtained from ground-based observations. The library consists of 27 stars of different spectral type, obtained by M. Franx at the 4m telescope of the KPNO with the RC Spectrograph (see van der Marel & Franx 1993 for more details on this template library). The spectra were rebinned logarithmically to the same scale as the galaxy spectra, and were shifted to a common velocity. The spectra cover the wavelength range  $4836 - 5547\text{\AA}$ . Although this range is smaller than that covered by the FOS spectra, it is centred on the Mg b triplet ( $\sim 5170\text{\AA}$ ), which is the most useful wavelength range for stellar kinematic analysis. The other strong feature in the FOS spectra, the NaD line, can be influenced by absorption from the interstellar medium, and is not a good absorption line for kinematic analysis.

Given the relative low *S/N* of the FOS spectra, we decided to construct one optimal template spectrum for each galaxy, rather than for each separate spectrum. For this purpose, we constructed a grand total spectrum of each galaxy, by summing all spectra at different aperture positions. We determined the best-fitting stellar mix using the same method as described in Section 3.4. For both NGC 4342 and NGC 4570 we found the best-fitting template mix to consist of giants and dwarfs of spectral types

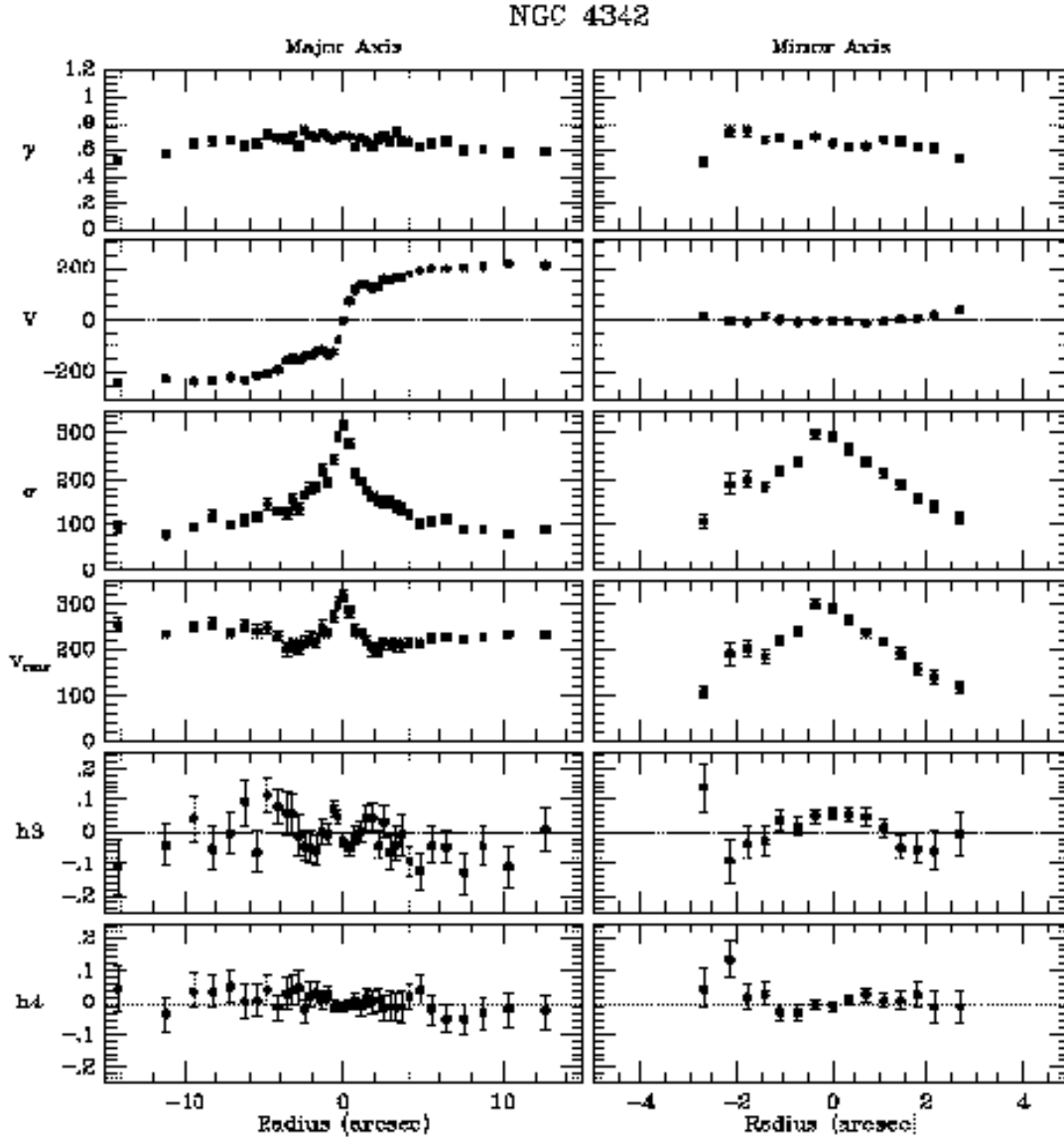


**Figure 10.** Major and minor axis stellar kinematics of NGC 4342 inferred from the WHT spectra. The panels show, from top to bottom: the line strength  $\gamma$ , the rotation velocity  $V$ , the velocity dispersion  $\sigma$ , the RMS projected line-of-sight velocity  $V_{\text{rms}} \equiv \sqrt{V^2 + \sigma^2}$ , and the Gauss-Hermite coefficients  $h_3$  and  $h_4$ . All velocities are in units of  $\text{km s}^{-1}$ . The scales on the abscissa are different for the major and minor axis data, as a result of the strong flattening of NGC 4342.

G and K.

## 5 STELLAR KINEMATICAL ANALYSIS

The accessible stellar kinematical information of galaxies is contained in the stellar line-of-sight velocity profiles (VPs). We expand each VP in a Gauss-Hermite series, following the approach of van der Marel & Franx (1993):

$$\text{VP}(v) = \frac{\gamma}{\sigma} \alpha(w) \left( 1 + \sum_{j=3}^N h_j H_j(w) \right), \quad (2)$$

where

$$\alpha(w) \equiv \frac{1}{\sqrt{2\pi}} e^{-\frac{1}{2}w^2}, \quad w \equiv (v - V)/\sigma. \quad (3)$$

Here  $v$  is the line-of-sight velocity,  $H_j$  are the Hermite polynomials of degree  $j$ , and  $h_j$  are the Gauss-Hermite coefficients. The first term in equation (2) represents a Gaussian with line strength  $\gamma$ , mean radial velocity  $V$ , and velocity dispersion  $\sigma$ . The even Gauss-Hermite coefficients quantify symmetric deviations of the VP from the best fitting Gaussian, and the odd coefficients quantify anti-symmetric deviations.

We determined the best-fitting VP parameters for each galaxy spectrum by  $\chi^2$ -minimization of the difference between the galaxy spectrum and a broadened template spectrum (using the Gauss-Hermite series as the broadening function). The fitting can be done either in Fourier space (e.g., van der Marel & Franx 1993) or in pixel space (e.g., van der Marel 1994). We adopted the latter approach, because it

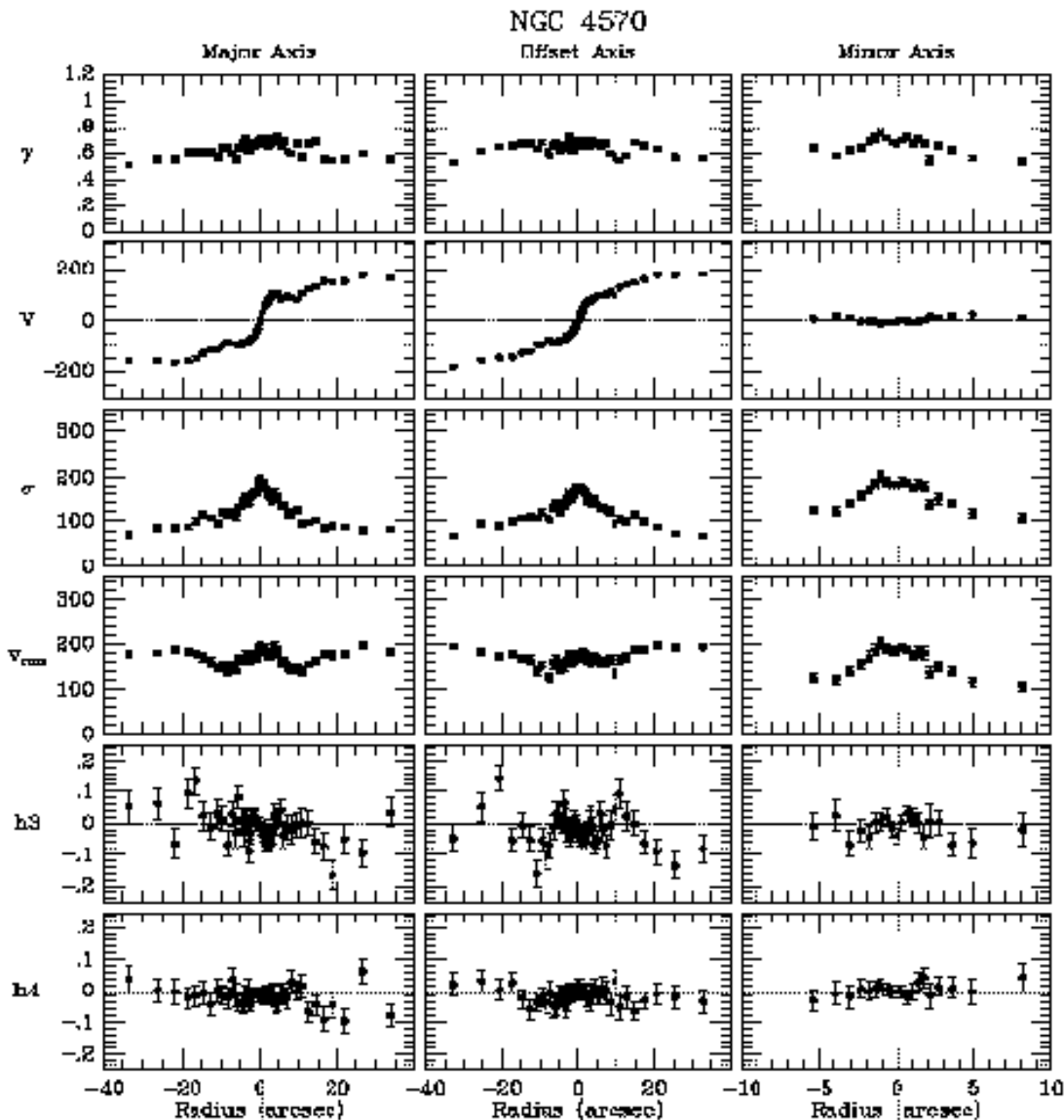


Figure 11. Same as Figure 10, but now for the major axis, offset axis (see Table 4), and minor axis of NGC 4570.

allows straightforward masking of sky lines (which are especially abundant in the WHT Ca II triplet spectra) and bad pixel regions (e.g., due to dead or noisy diodes in the FOS spectra). However, we also performed Fourier-space fitting for all spectra, as a consistency check, and found excellent agreement in all cases.

### 5.1 The WHT spectra

The stellar kinematical results obtained from the WHT spectra are shown in Figures 10 and 11, for NGC 4342 and NGC 4570, respectively, and are listed in the tables of Appendix B. Prior to analysis, the spectra were spatially rebinned along the slit to a  $S/N \geq 20$  per  $10 \text{ km s}^{-1}$ . As template we used the optimal mix of stellar spectra determined as described in Section 3.4.

The kinematics of both galaxies are remarkably similar. Each galaxy shows rapid rotation along the major

axis, no measurable rotation along the minor axis, and a central peak in the velocity dispersion profile. The central dispersion measured for NGC 4342 is  $317 \text{ km s}^{-1}$ ; that for NGC 4570 is  $198 \text{ km s}^{-1}$ . The central velocity dispersion of NGC 4342 is extremely high. Only very few galaxies have central velocity dispersions, measured from the ground, that are larger than, or comparable to that of NGC 4342; examples are: M87 (van der Marel 1994), NGC 3115 (Kormendy & Richstone 1992) and NGC 4594 (Kormendy 1988; van der Marel et al. 1994). These galaxies are all strong candidates for harbouring a massive nuclear black hole. The latter two galaxies are S0s, and have rather similar kinematics as NGC 4342 and NGC 4570.

The observed rotation curve shapes are typical for S0 galaxies (e.g., Simien, Michard & Prugniel 1992; Fisher 1997). They are steep in the centre, show a dip at intermediate radii, and then rise more gradually out to the last measured point. The dip is also present in the radial pro-

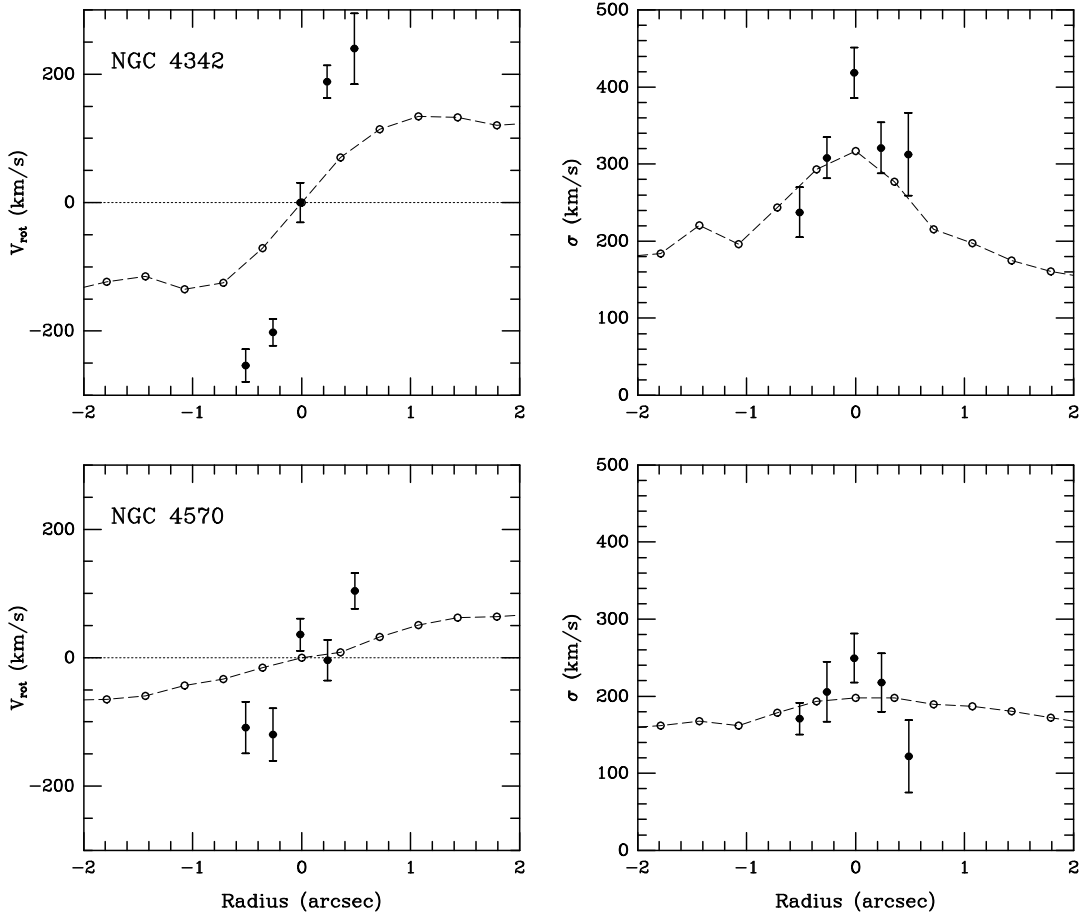


**Figure 12.** Major axis rotation velocities  $V$  (left) and velocity dispersions  $\sigma$  (right) for the nuclear regions of NGC 4342 (top) and NGC 4570 (bottom), inferred from the HST/FOS spectra (data points with error bars). For comparison, the open circles connected by dashed lines show the lower-spatial resolution results from the WHT spectra.

file of the rms-velocity,  $V_{\text{rms}} = \sqrt{V^2 + \sigma^2}$ . For NGC 4342, the radial profile of  $h_3$  also shows an interesting feature. Although the profile is somewhat noisy, it appears that  $h_3$  changes its sign in the radial region where the dip in the rotation curve occurs. This has in fact been observed in a number of other S0s as well (Fisher 1997). Most likely, all these kinematical features reflect radial changes in the relative contributions of the different structural components. The even Gauss-Hermite coefficient  $h_4$ , expressing symmetric deviations of the VP from a Gaussian, is never significantly different from zero.

## 5.2 The HST spectra

From the HST/FOS spectra we determined only the mean velocity and velocity dispersion of the best-fitting Gaussian VPs. The spectra are not of sufficient  $S/N$  to determine the deviations from a Gaussian shape. A complication in the kinematical analysis is provided by the fact that we must use a template spectrum that was obtained with a different instrument (Section 4.5). This implies that the template and galaxy spectra do not have the same line-spread-function (LSF; i.e., the observed response for a single monochromatic line). The parameters  $\tilde{V}$  and  $\tilde{\sigma}$  obtained from the kinematical analysis must be corrected for these LSF differences, to

obtain unbiased estimates for the true mean stellar velocity  $V$  and velocity dispersion  $\sigma$ . The required corrections can be made, since the LSFs of both the galaxy and template spectra can be measured and/or calculated. Our approach for this is described in detail in Appendix A. The kinematical results obtained after correction for LSF differences are listed in Table 5. Figure 12 shows the results for the apertures that were centered on the major axis, as function of major axis distance. The systemic velocity for each galaxy was estimated as the mean velocity at  $r = 0$ , obtained by linearly interpolating the rotation curve between aperture positions #4 and #5.

For NGC 4342, the FOS spectra show a much higher central velocity dispersion than the lower spatial resolution WHT spectra,  $\sigma_0 = 418 \text{ km s}^{-1}$  vs.  $\sigma_0 = 320 \text{ km s}^{-1}$ , respectively. Also, a very steep central rotation gradient is measured with the FOS, much steeper than that measured from the ground. The rotation velocity reaches  $V_{\text{rot}} \approx 200 \text{ km s}^{-1}$  at  $0.25''$  from the centre (corresponding to 18 pc at a distance of 15 Mpc). These observations suggest the presence of a strong central mass concentration in NGC 4342, possibly a massive black hole. We will address this issue in a forthcoming paper through detailed dynamical models.

For NGC 4570, the FOS results are somewhat more difficult to interpret. There is certainly much less of a sug-

gestion for a central mass concentration on the basis of the qualitative features of the data. The central velocity dispersion is larger than measured from the ground, but only by a marginal amount. As for NGC 4342, the rotation curve is steeper than measured from the ground, but the scatter between neighbouring points (especially observations B1 and B2), suggests the possible presence of small systematic errors. No known error could be identified, but we cannot exclude GIMP-related wavelength offsets of several tens of  $\text{km s}^{-1}$  between different spectra (cf. Section 4.4). Such offsets are not a problem for the NGC 4342 spectra, for which our wavelength calibration is more accurate.

## 6 STELLAR POPULATIONS

In this section we investigate the stellar populations of NGC 4342 and NGC 4570, by studying broad-band colour images (Section 6.1) and line strengths indices (Section 6.2). The results are compared to models to study the age and metallicity of the populations (Section 6.3). This allows us to address the formation of the nuclear discs, and to discuss the evidence for either coeval or secular formation.

### 6.1 Broad-band colour images

Fisher, Franx & Illingworth (1996) presented  $B - R_c$  colour images of  $148'' \times 148''$  for a number of close to edge-on S0s. They found that the  $B - R_c$  contours are flatter than the isophotes; i.e., whereas the colour gradients along the minor axis decrease outwards, the major axis colour gradients flatten out towards larger radii. Similar behaviour was found for the Mg2 line strength gradients. The  $H\beta$  gradients, however, were found to be rather flat throughout the entire galaxy. These findings suggest that the (outer) discs of S0s are more metal rich than their bulges, therewith contradicting formation scenarios in which the bulges are formed from heated disc material.

We constructed  $U - V$  and  $V - I$  colour images from the HST/WFPC2 data. To take into account that the PSFs are significantly different for the three bands, we convolved the  $U$ -band image with the  $V$ -band PSF, the  $I$ -band image with the  $V$ -band PSF, and the  $V$ -band image with either the  $U$ -, or  $I$ -band PSF (using PSFs constructed with the Tiny-Tim software package). This approach degrades the spatial resolution of the colour images somewhat, but provides the safest way to avoid systematic colour errors near the centre.

Figure 13 presents contour maps of the  $V - I$  colour images (thick contours), superimposed on contour maps of the  $V$ -band images (thin contours). The images only go out to  $\sim 10''$ , and within this limited extent, both the bulge and the outer disc add significantly to the projected surface brightness. A determination of the colours of the individual components is therefore not straightforward. Nonetheless, our results clearly show that the colour contours are flatter than the isophotes. Similar results were obtained for the  $U - V$  images. Our results are therefore at least qualitatively consistent with those of Fisher, Franx & Illingworth (1996).

Our high spatial resolution colour images are best suited to study population differences between the bulges and the *nuclear* discs of both galaxies. If these components had the same, uniform stellar population, then the flattening of the colour contours and the isophotes in the central arcsec would

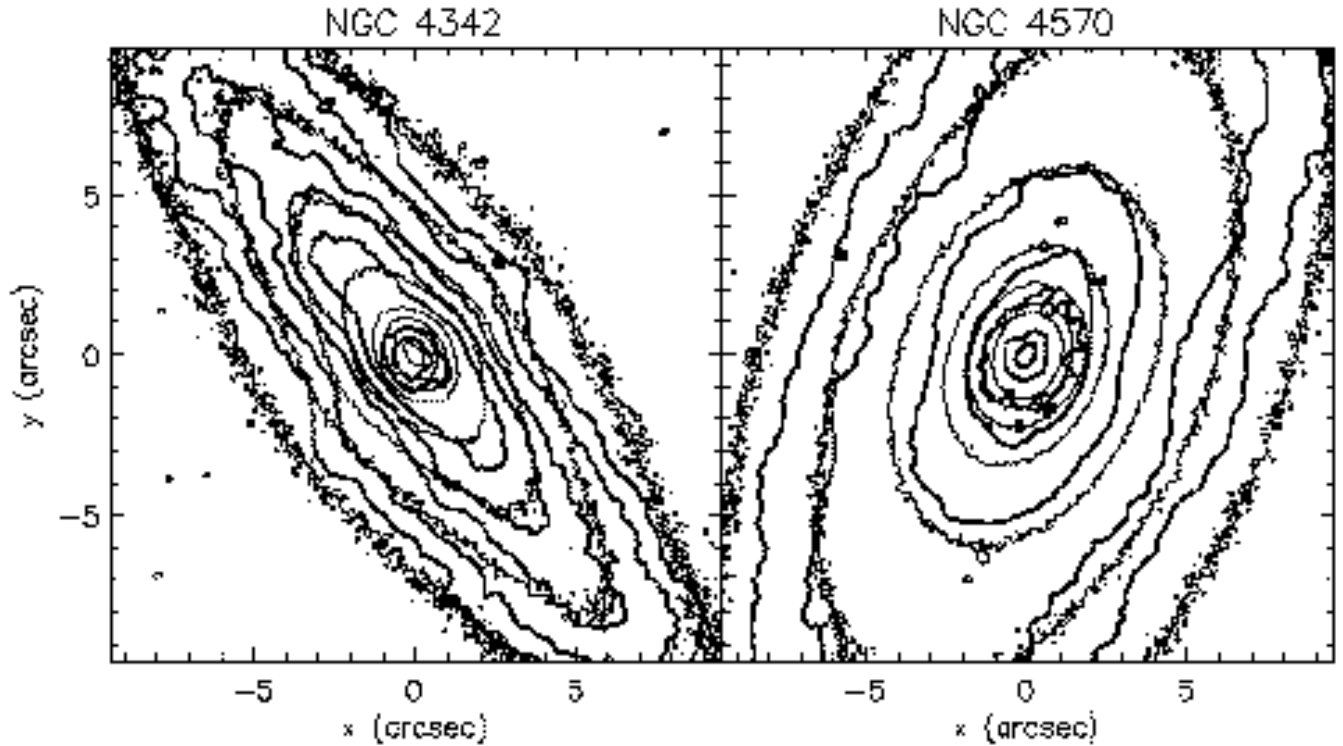
have to be similar. This is exactly what is observed, and contrasts strongly with the results at larger radii. Thus, the colour images do not suggest a clear difference in colour between the nuclear discs and the central regions of the bulges in either of the two galaxies. However, one has to keep in mind that broad band colours are rather poor population diagnostics (Worthey 1994), in that different populations can have similar broad band colours (see e.g., Figure 15 below). Therefore, we cannot rule out that a more detailed analysis may yet reveal some subtle population differences. In Section 6.2 below we probe the stellar populations of the nuclear regions in NGC 4342 and NGC 4570 through their absorption line strengths.

Figure 14 shows the  $U - V$  and  $V - I$  colour gradients as a function of major axis radius. There is a marked difference between the two galaxies. NGC 4342 shows no clear colour-gradients inside  $\sim 0.3''$  and outside  $\sim 3''$ . Around  $\sim 1''$  we find  $\Delta(U - V)/\Delta \log r = -0.26 \pm 0.02$  and  $\Delta(V - I)/\Delta \log r = -0.05 \pm 0.01$ . By contrast, NGC 4570 shows strong gradients over the entire radial interval studied:  $\Delta(U - V)/\Delta \log r$  ranges from  $-0.41 \pm 0.02$  at the outside, to  $-0.21 \pm 0.02$  in the centre;  $\Delta(V - I)/\Delta \log r$  has more or less a constant value of  $-0.06 \pm 0.01$  from the centre out to  $\sim 20''$ . The  $U - V$  gradient at the outside of NGC 4570 is extremely large as compared with those of other early-type galaxies (cf. Peletier 1989).

The central reddening typical of early-type galaxies is generally interpreted as due to a metallicity gradient. The best evidence for this comes from spectroscopic measurements of absorption lines in ellipticals (e.g., Faber 1977; Burstein et al. 1984; Efstathiou & Gorgas 1985; Peletier 1989). Several studies have found a correlation between colour (and line strength) gradients and total luminosity. For low-mass galaxies ( $M_B > -20.5$ ), the gradients increase with the total mass of the galaxy (e.g., Vader et al. 1988; Carollo, Danziger & Buson 1993), consistent with the predictions of simple models of dissipative collapse coupled with supernovae-induced winds (Larson 1974; Carlberg 1984; Arimoto & Yoshii 1987; Matteucci & Tornambè 1987). For NGC 4342 and NGC 4570, the presence of both an outer and a nuclear disc indeed indicates that dissipation has played a role during their formation. The morphology of these galaxies is very similar, but NGC 4570 is almost 1.6 magnitudes brighter. This indicates that NGC 4570 is 4.2 times more massive, assuming that both galaxies have a similar mass-to-light ratio. The finding that the colour gradients in NGC 4570 are larger than those in NGC 4342 is therefore qualitatively consistent with dissipative galaxy formation, in which star formation lasts longer and the onset of a galactic wind starts later, in higher mass galaxies.

### 6.2 Line strengths

Line strength measurements provide additional information about ages and metallicities that is complementary to, and often more accurate than, that provided by broad-band colours. The most commonly used spectral indices are those of the Lick-IDS system (Faber et al. 1985; Worthey et al. 1994), in particular  $H\beta$ , Mg2, Mgb, Fe5270 and Fe5335. These are all in the wavelength range 4800–5400Å, which is included in the FOS spectra. The  $S/N$  of the FOS spectra was not sufficient to infer line strengths at each aper-



**Figure 13.** Contour plots of  $V - I$  (thick contours), superimposed on isophotal  $V$ -band contours (thin contours). In both galaxies, the outermost colour isophote corresponds to  $V - I = 1.22$ . Subsequent contours are 0.02 mag redder. For NGC 4342, the inner four contours step by only 0.01 mag, in order to better sample the small colour gradient in this galaxy (see Figure 14). The colour images were smoothed to suppress noise, while maintaining the information in the images. At large radii, the colour contours are flatter than the isophotal contours. In the central region, the flattening of both contours is similar. The dents in the  $V - I = 1.30$  contour of NGC 4570 are caused by the relatively blue colours of the two features marked 'A' and 'B' in Figure 6 (see van den Bosch & Emsellem 1997, for a discussion on the nature of these features).

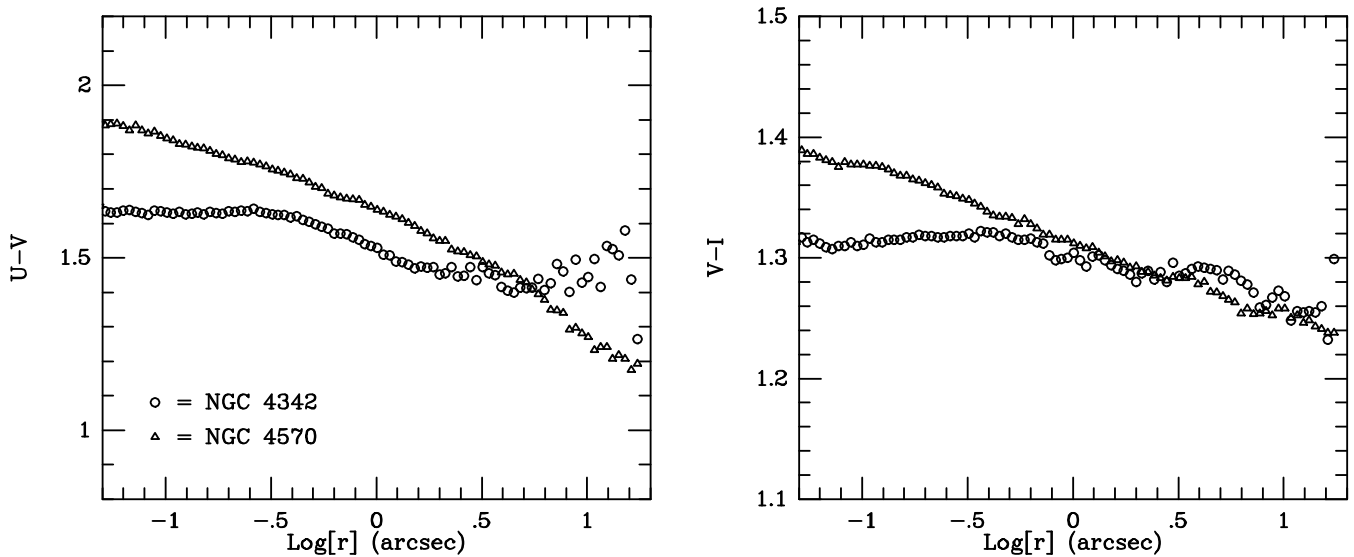


**Figure 14.** Major-axis  $U - V$  and  $V - I$  colour gradients, as a function of radius, for NGC 4342 and NGC 4570. The behaviour of the gradients is markedly different for the two galaxies.

ture position individually, and we therefore measured line strength indices from one grand-total spectrum for each galaxy, obtained by summing the different spectra available for each galaxy. Two corrections have to be applied

to these indices. First, they must be corrected for the broadening effect of velocity dispersion, which weakens most of the lines. We determined empirical correction factors,  $C(\sigma) \equiv \text{index}(0)/\text{index}(\sigma)$ , for each of the 5 indices listed



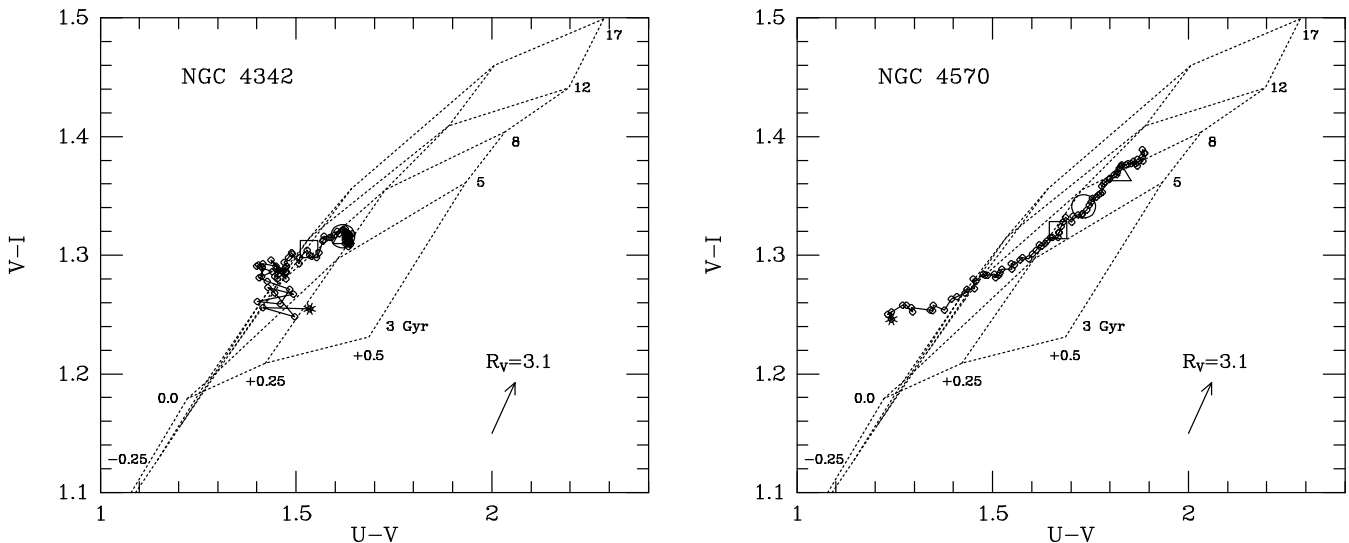


**Figure 15.** Colour-colour diagrams for NGC 4342 and NGC 4570. Small circles connected by solid lines show the colours for isophotes of different radii; the outermost isophote is indicated by an asterisk. Large symbols indicate the average colours of the nucleus (triangle), nuclear disc (circle) and bulge (square). Overplotted as dotted lines are the predictions of the single-burst stellar population models of Worthey (1994), for a grid of age (3–17 Gyr) and metallicity ( $[\text{Fe}/\text{H}] = -0.25 - +0.5$ ) values. The lines for  $[\text{Fe}/\text{H}] = -0.25$  and  $[\text{Fe}/\text{H}] = 0$  partly overlay each other, indicating a degeneracy between metallicity and age at low metallicities. The arrow indicates the slope of dust reddening for  $R_V \equiv A(V)/E(B - V) = 3.1$ , as typical for Galactic dust.

**Table 6.** Line strength indices

	NGC 4342	NGC 4570
Mg2	$0.338 \pm 0.087$	$0.386 \pm 0.015$
H $\beta$	$1.52 \pm 0.30$	$2.51 \pm 0.48$
Mgb	$5.11 \pm 0.33$	$5.32 \pm 0.53$
Fe5270	$2.94 \pm 0.37$	$3.38 \pm 0.60$
Fe5335	$3.29 \pm 0.42$	$3.40 \pm 0.67$

Line strength indices and errors for the central regions of NGC 4342 and NGC 4570 (corrected for velocity dispersion broadening and converted to the Lick-IDS system), derived from grand-total FOS spectra as described in the text.

above;  $\text{index}(0)$  is the index measured from the template star K193,  $\sigma$  is the velocity dispersion of the grand-total spectrum derived using K193 as template, and  $\text{index}(\sigma)$  is the index of the K193 spectrum broadened with a Gaussian of dispersion  $\sigma$ . Second, to be able to compare our indices with the Worthey (1994) stellar population models (see Section 6.3), they must be converted to the Lick scale. This is necessary to correct for differences in the spectral resolution and in the spectral response function between our FOS data and the Lick group data. We compared the indices derived by us from the FOS spectrum of F193 with those obtained by the Lick group from observations of the same star (Worthey et al. 1994). This yields correction factors  $\text{index}(\text{LICK})/\text{index}(\text{FOS})$  for each of the four atomic indices. For the molecular Mg2 index, we used the difference  $[\text{index}(\text{LICK}) - \text{index}(\text{FOS})]$ . Table 6 lists the line strength indices thus obtained for NGC 4342 and NGC 4570, corrected for velocity dispersion broadening and converted to the Lick scale.

### 6.3 Comparison with stellar population models

To address the age and metallicity of the stellar populations in NGC 4342 and NGC 4570, we have compared their colours and line strengths to the single-burst stellar population models of Worthey (1994). These models give the fluxes, colours, and line strengths of an evolving stellar population, as a function of age and metallicity  $[\text{Fe}/\text{H}]$ , calculated from isochrones and model flux libraries of stars with a Salpeter (1955) initial mass function.

In Figure 15 we plot  $V - I$  vs.  $U - V$  for the two galaxies. Small open circles indicate results for isophotes at different radii; neighbouring isophotes are connected, and an asterisk indicates the outermost radius. Large symbols indicate the average colours of the nucleus (open triangle), the nuclear disk (open circle) and the bulge (open square). For the nucleus we used the region inside  $0.18''$ , for the nuclear disk we used the region along the major axis between  $0.18''$  and  $0.71''$  (which is where the nuclear discs most clearly stand out from the isophotal analysis, cf. Figures 4 and 5), and for the bulge we used the region inside  $0.71''$ , but offset from the major axis by  $0.5'' - 0.6''$ . Overplotted in Figure 15 are the predictions of Worthey’s models for an age-metallicity grid, with ages between 3 and 17 Gyr, and  $[\text{Fe}/\text{H}]$  between  $-0.25$  and  $+0.50$ . For  $[\text{Fe}/\text{H}] \lesssim +0.25$  there is strong degeneracy between age and metallicity, as the grid points crowd together. However, for high metal abundances the  $V - I$  vs.  $U - V$  diagram is a useful discriminator between age and metallicity effects.

For NGC 4342, the main body of the galaxy lies close to the 8 Gyr, solar-metallicity grid point. The nucleus and nuclear disc have different colours than the main body, but have similar colours to each other (cf. Figure 15). Their colours are well fit with a similar age as the main body, but with a somewhat higher metallicity ( $[\text{Fe}/\text{H}] \approx +0.25$ ).

There is considerable uncertainty in these results though, since most points fall in the region of the model grid where there is a strong age-metallicity degeneracy.

The colour-colour diagram of NGC 4570 is very different. The colours change dramatically from the outermost point to the very nucleus. Whereas the outermost points fall outside the grid of Worthey’s models, the nucleus is consistent with an 8 Gyr old population with  $[\text{Fe}/\text{H}] \approx +0.35$ . The run of the central isophotes in the colour-colour diagram has a similar slope as would be expected from reddening due to dust (as indicated by the arrow in Figure 15), but dust reddening is not likely to be the cause of the observed gradients: both the isophotes and the colour-images are very smooth, and no  $100\mu\text{m}$  emission has been detected. It would be tempting to interpret the observed colour differences between the nucleus, nuclear disc, and bulge as due to changes in age. However, the nuclear disc does not show up as a separate component in the colour images. The colour differences therefore most likely reflect mere changes in stellar population with radius from the centre, rather than differences between separate components.

From the line indices listed in Table 6, we can calculate the new index  $[\text{MgFe}]$ , which is defined as  $\sqrt{\text{Mgb}\langle\text{Fe}\rangle}$ , where  $\langle\text{Fe}\rangle = (\text{Fe}5270 + \text{Fe}5335)/2$ . This index is often used as a metallicity indicator (e.g., González 1993). We derive  $\log [\text{MgFe}] = 0.60 \pm 0.04$  and  $0.63 \pm 0.06$ , for NGC 4342 and NGC 4570, respectively. The  $\text{H}\beta$  index is a sensitive age-indicator. Figure 16 shows  $\text{H}\beta$  vs.  $[\text{MgFe}]$  for each galaxy, with overplotted the predictions of Worthey’s stellar population models. The observed indices refer to the central region ( $\lesssim 0.5''$ ) of each galaxy. The models indicate that this central region in NGC 4342 has a high metallicity ( $[\text{Fe}/\text{H}] \approx +0.35$ ) and an age of  $\sim 8$  Gyr. This is roughly consistent with the age and metallicity found from the broad band colours (see Figure 15). The indices for NGC 4570, on the other hand, fall outside the model grid. The high  $\text{H}\beta$  index suggests a very young stellar population, whereas both the colours and the value of  $[\text{MgFe}]$  suggest a high metallicity.

Although these results are suggestive, we do not wish to draw very strong conclusions. The error bars on the measured line indices are large, due to the low  $S/N$  of the FOS spectra. We have been careful and conservative in the determination of these errors, but note that it is very difficult to quantify possible systematic errors. In addition, the age and metallicity values inferred from the line strengths refer only to the nuclear region  $\lesssim 0.5''$ , and not necessarily to the entire bulge population. Fisher, Franx & Illingworth (1996) have shown that the nuclear regions of S0s are typically a few Gyr younger than the bulk of the galaxy. Also, ages measured from the  $\text{H}\beta$  index have to be interpreted with care. First, the observed  $\text{H}\beta$  index could be dominated by horizontal branch stars, rather than by main-sequence turnoff stars. In this case it would be more sensitive to variations in the initial mass function, than to variations in age. Second, the  $\text{H}\beta$  index is very sensitive to small numbers of young stars present. The relatively young age inferred for the nuclear population in NGC 4570 may therefore reflect merely the most recent generation of stars, rather than the age of the entire, presumably much older generation. Indeed, van den Bosch & Emsellem (1997) present evidence that the central region of NGC 4570 has had recent star formation. A

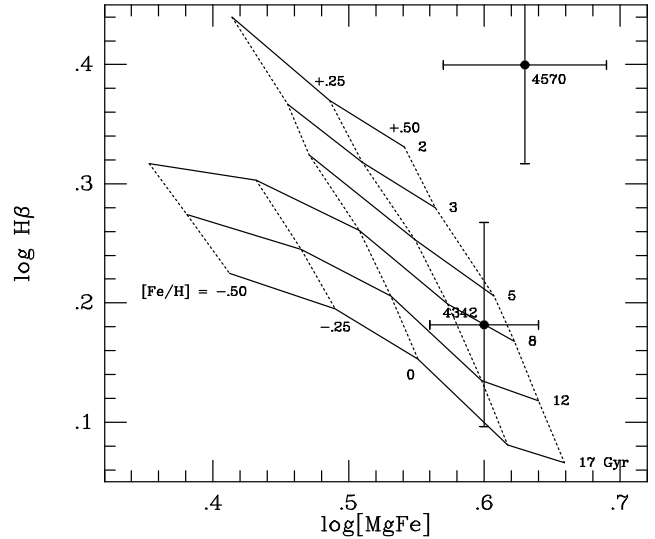


**Figure 16.** Diagram of the age indicator  $\text{H}\beta$  vs. the metallicity indicator  $[\text{MgFe}]$ . Data points with error bars indicate the measurements from the grand-total FOS spectra. Overplotted as dotted lines are the predictions of the single-burst stellar population models of Worthey (1994), for a grid of age (3–17 Gyr) and metallicity ( $[\text{Fe}/\text{H}] = -0.25$ – $+0.5$ ) values.

more thorough investigation of the stellar populations of the separate components in NGC 4243 and NGC 4570 than presented here will have to await additional observations of line indices, both at larger radii from the centre and with higher  $S/N$ .

## 7 CONCLUSIONS AND DISCUSSION

Small stellar discs embedded in the nuclei of early-type galaxies are intriguing: they contain clues about the process of galaxy formation, and their dynamics provide a useful tool to constrain the central mass distribution. We have presented high spatial resolution photometric and spectroscopic data for two E/S0 galaxies in the Virgo cluster, NGC 4342 and NGC 4570, for which pre-refurbishment HST images showed nuclear discs in addition to larger outer discs. New HST/WFPC2 images confirm the existence of the nuclear discs, and dismiss suggestions that the earlier detections were artifacts of Lucy deconvolution; the new images clearly show the discs even without deconvolution. The decomposition of both galaxies in disc and bulge components will be presented in a forthcoming paper (Scorza & van den Bosch 1997). Here we have focussed on using the multi-colour WFPC2 images, WHT spectra and HST/FOS spectra to do a first study of the stellar populations and dynamics of the nuclear discs.

Broad-band colour images were constructed from the WFPC2 data, properly taking into account the different PSFs in the different bands. For both galaxies we find the colour contours outside  $\sim 2''$  to be flatter than the isophotes. We have also determined the radial colour gradients in both galaxies. The gradients in the more massive galaxy NGC 4570 are larger than those for NGC 4342, consistent with the predictions of simple models of dissipative collapse coupled with supernovae-induced galactic winds. All these results are in good agreement with those of Fisher, Franx

& Illingworth (1997), who studied the ages and metallicities of a sample of 20 S0s, and seem to suggest that the bulges of S0s are not formed out of heated disc stars, but are most likely the results of dissipational formation. By contrast, from the colour images and gradients inside  $\sim 2''$  we find no strong evidence for population differences between the bulges and the *nuclear* discs in both galaxies.

We have measured line strength indices for several diagnostic lines from the summed FOS spectra, to obtain additional stellar population information about the nuclear ( $\lesssim 0.5''$ ) components of both galaxies. Comparison with the single-burst stellar population models of Worthey (1994) indicates that the central regions of both galaxies have metallicities  $[\text{Fe}/\text{H}] \approx +0.25$  or larger. NGC 4342 is well fit with an age of  $\sim 8$  Gyr. NGC 4570 has an unusually large  $\text{H}\beta$  line strength, which may be suggestive of recent star formation. In van den Bosch & Emsellem (1997) evidence is presented that the central region of NGC 4570 has experienced bar induced secular evolution. Unfortunately, neither the broad band colours nor the line strength measurements presented here, place important constraints on possible formation scenarios for the nuclear discs. Additional observations of line indices, both at larger radii from the centre and with higher  $S/N$ , are required for a more thorough investigation of the stellar populations of the separate components in these galaxies.

The WHT and FOS spectra were used to determine the nuclear stellar kinematics of NGC 4342 and NGC 4570. The dynamical structure of both galaxies is found to be remarkably similar to that of other well-studied S0s, such as NGC 3115 (Kormendy & Richstone 1992), NGC 4026 and NGC 4111 (Simien, Michard & Prugniel 1993; Fisher 1997). The long-slit WHT spectra have high  $S/N$  and a large radial extent. They reveal a very centrally peaked velocity dispersion profile in both galaxies. The rotation curves clearly show the different dynamical properties of the structural components identified photometrically. The single-aperture FOS spectra of the nuclear regions of both galaxies have lower  $S/N$  than the WHT spectra, but have four times higher spatial resolution. The FOS data of NGC 4342 show significantly higher velocities than the WHT data. The observed central velocity dispersion is  $\sim 420 \text{ km s}^{-1}$ , compared to ‘only’  $\sim 320 \text{ km s}^{-1}$  as measured from the WHT spectra. The rotation velocity reaches  $\sim 200 \text{ km s}^{-1}$  at  $0.25''$ , implying a much steeper rotation gradient than inferred from the WHT data. These observations indicate a high central mass density. Detailed dynamical models to be presented in a forthcoming paper (Cretton & van den Bosch 1997, see also van den Bosch & Jaffe 1997) provide strong evidence for the presence of a few times  $10^8 M_{\odot}$  black hole in NGC 4342. The FOS data for NGC 4570 are more difficult to interpret. The rotation curve is considerably steeper than measured from the ground, but there is some indication for possible systematic errors. The central velocity dispersion is larger than measured from the ground, but only marginally so. Although these data certainly do not exclude the possible presence of a black hole in NGC 4570, the qualitative features of the data do not suggest such a black hole as strongly as they do for NGC 4342.

## ACKNOWLEDGMENTS

The observations presented in this paper were obtained with the NASA/ESA Hubble Space Telescope and with the William Herschel Telescope. HST data are obtained at the Space Telescope Science Institute, which is operated by AURA, Inc., under NASA contract NAS 5-26555. The WHT is operated on the island of La Palma by the Royal Greenwich Observatory in the Spanish Observatorio del Roque de los Muchachos of the Instituto de Astrofísica de Canarias. We are grateful to Eric Emsellem for his help with the MGE analysis, and to Marijn Franx for providing a ground-based template library. RpvM was supported by a Hubble Fellowship, #HF-1065.01-94A, awarded by STScI.

## REFERENCES

- Arimoto N., Yoshii Y., 1987, *A&A*, 173, 23  
 Bender R., Döbereiner S., Möllenhoff C., 1988, *A&AS*, 74, 385  
 Burrows C.J. et al., 1995, *Hubble Space Telescope Wide Field and Planetary Camera 2 Instrument Handbook*, Version 3.0. STScI, Baltimore  
 Burstein D., 1979, *ApJ*, 234, 435  
 Burstein D., Faber S.M., Gaskell C.M., Krumm N., 1984, *ApJ*, 287, 586  
 Carlberg R.C., 1984, *ApJ*, 286, 403  
 Carollo C.M., Danziger I.J., Buson L., 1993, *MNRAS*, 265, 553  
 Cretton N., van den Bosch F.C., 1997, in preparation  
 de Vaucouleurs G., de Vaucouleurs A., Corwin H.C., 1976, *Second Reference Catalogue of Bright Galaxies*. University of Texas, Austin (RC2)  
 Dressler A., 1984, *ApJ*, 286, 97  
 Efsthathiou G., Gorgas J., 1985, *MNRAS*, 215, 37p  
 Emsellem E., Monnet G., Bacon R., 1994, *A&A*, 285, 723  
 Evans I.N., 1995, *FOS Instrument Science Report CAL/FOS-140*, ‘Post-COSTAR FOS small aperture relative throughputs derived from SMOV data’. STScI, Baltimore  
 Faber S.M., 1977, in Tinsley B.T., Larson R.B., eds., *The Evolution of Galaxies and Stellar Populations*, Yale University Press, New Haven, p. 157  
 Faber S.M., Friel E., Burstein D., Gaskell C.M., 1985, *ApJS*, 57, 711  
 Fisher D., Franx M., Illingworth G.D., 1996, *ApJ*, 459, 110  
 Fisher D., 1997, *AJ*, 113, 950  
 Forbes D.A., 1994, *AJ*, 107, 2017  
 Gebhardt K. et al., 1996, *AJ*, 112, 105  
 González J.J., 1993, *PhD Thesis*. University of California, Santa Cruz  
 Holtzman J.A. et al., 1995a, *PASP*, 107, 156  
 Holtzman J.A. et al., 1995b, *PASP*, 107, 1065  
 Jacoby G., Ciardullo R., Ford H.C., 1990, *ApJ*, 356, 332  
 Jaffe W., Ford H.C., Ferrarese L., van den Bosch F.C., O’Connell R.W., 1994, *AJ*, 108, 1567  
 Jedrzejewski R.I., 1987, *MNRAS*, 226, 747  
 Keyes T. et al., 1995, *Hubble Space Telescope Faint Object Spectrograph Instrument Handbook*, Version 6.0. STScI, Baltimore  
 Knapp G.R., Guhathakurta P., Kim D.-W., Jura M., 1989, *ApJS*, 70, 329  
 Kormendy J., 1988, *ApJ*, 335, 40  
 Kormendy J., Richstone D.O., 1992, *ApJ*, 393, 559  
 Kuijken K., Merrifield M.R., 1993, *MNRAS*, 264, 712  
 Larson R.B., 1974, *MNRAS*, 166, 385  
 Lauer T.R., 1985, *MNRAS*, 216, 429  
 Lauer T.R. et al., 1995, *AJ*, 110, 2622  
 Lucy L.B., 1974, *AJ*, 74, 745  
 Matteucci F., Tornambè A., 1987, *A&A*, 185, 51

- Michard R., 1996, *A&AS*, 117, 583  
 Nieto J.-L., Bender R., Arnaud J., Surma P., 1991, *A&A*, 244, L25  
 Peletier R.F., 1989, PhD Thesis. University of Groningen  
 Rix H.-W., White S.D.M., 1992, *MNRAS*, 254, 389  
 Sargent W.L.W., Young P.J., Bokserberg A., Shortridge K., Lynds C.R., Hartwick F.D.A., 1978, *ApJ*, 221, 731  
 Scorza C., Bender R., 1990, *A&A*, 235, 49  
 Scorza C., Bender R., 1995, *A&A*, 293, 20  
 Scorza C., van den Bosch F.C., 1997, in preparation  
 Simien F., Michard R., Prugniel P., 1993, in Danziger I.J., Zeilinger W.W., Kj ar K., eds., *Structure, Dynamics and Chemical Evolution of Elliptical Galaxies*. ESO Conference and Workshop Proceedings, Garching bei M unchen, p. 211  
 Tonry J.L., Davis M., 1979, *AJ*, 84, 1511  
 Vader J.P., Vigroux L., Lach eze-Rey M., Souviron J., 1988, *A&A*, 203, 217  
 van den Bosch F.C., Ferrarese L., Jaffe W., Ford H.C., O’Connell R.W., 1994, *AJ*, 108, 1579  
 van den Bosch F.C., de Zeeuw P.T., 1996, *MNRAS*, 283, 381  
 van den Bosch F.C., Jaffe W., 1997, in Arnaboldi M., Da Costa G.S., Saha P., eds., *The Nature of Elliptical Galaxies*, A.S.P. Conference Series Volume 116, p. 142  
 van den Bosch F.C., Emsellem E., 1997, *MNRAS*, submitted  
 van der Marel R.P., 1991, *MNRAS*, 253, 710  
 van der Marel R.P., 1994, *MNRAS*, 270, 271  
 van der Marel R.P., Franx M., 1993, *ApJ*, 407, 525  
 van der Marel R.P., Rix H.-W., Carter D., Franx M., White S.D.M., de Zeeuw P.T., 1994, *MNRAS*, 268, 521  
 van der Marel R.P., de Zeeuw P.T., Rix H.-W., 1997, *ApJ*, in press  
 Worthey G., 1994, *ApJS*, 95, 107  
 Worthey G., Faber S.M., Gonz alez J.J., Burstein D., 1994, *ApJS*, 94, 687  
 Wrobel J.M., 1991, *AJ*, 101, 127

## APPENDIX A: LSF CORRECTIONS FOR THE HST/FOS SPECTRA

### A.1 Basic equations

For each galaxy there are seven HST/FOS galaxy spectra,  $G_i$  ( $i = 1, \dots, 7$ ). Each spectrum is the convolution of the stellar velocity profile,  $VP_i$ , the characteristic stellar spectrum of the population of the galaxy,  $S_G$ , and the line-spread-function of the observation,  $LSF_i$ :

$$G_i = VP_i \otimes S_G \otimes LSF_i. \quad (A1)$$

We assume that each  $VP_i$  is a Gaussian with mean velocity  $V_i$  and velocity dispersion  $\sigma_i$ . The template spectrum,  $T$ , is the convolution of the stellar spectral mix,  $S_T$ , and the line-spread-function of the template star observations,  $LSF_T$ :

$$T = S_T \otimes LSF_T. \quad (A2)$$

The stellar kinematical analysis minimizes

$$\chi^2 = \int [G_i - (T \otimes \widetilde{VP}_i)]^2, \quad (A3)$$

to find the parameters  $\widetilde{V}_i$  and  $\widetilde{\sigma}_i$  of the best-fitting Gaussian broadening function  $\widetilde{VP}_i$ . It is generally assumed that there is no template mismatch, i.e.,  $S_T = S_G$ .

If the LSFs of the galaxy and template spectra are identical,  $LSF_i \equiv LSF_T$ , as is usually assumed if all observations are obtained with the same instrument, then  $\widetilde{V}_i$  and  $\widetilde{\sigma}_i$  are unbiased estimates of the true mean velocity  $V_i$  and velocity

dispersion  $\sigma_i$ . In our case the galaxy and template spectra were not obtained with the same instrument, and hence the LSFs cannot be assumed to be identical. Thus,  $\widetilde{V}_i$  and  $\widetilde{\sigma}_i$  must be corrected for the LSF differences between the galaxy and template spectra, to obtain proper estimates for  $V_i$  and  $\sigma_i$ .

### A.2 The HST line-spread-functions

For HST/FOS observations one may assume (van der Marel 1997) that the LSF for observation  $i$ ,  $LSF_i$ , is the convolution of the normalized intensity distribution of the light that falls onto the grating,  $A_i$ , and the instrumental line-broadening function due to the grating and the detector resolution,  $H$ :

$$LSF_i = A_i \otimes H, \quad (A4)$$

The illumination function  $A_i$  is a function of the unconvolved, projected light distribution of the galaxy, the aperture position, and the kernel function that describes the HST/FOS PSF and the aperture geometry. These are all known: the MGE fits in Table 3 describe the unconvolved light distribution, the aperture positions ( $x_{ap}, y_{ap}$ ) for all observations are listed in Table 5, and the PSF+aperture kernel was derived in Section 4.2. The functions  $A_i$  can therefore be calculated explicitly for all galaxy observations.

One may write for any pair of observations at positions  $i$  and  $j$  within the same galaxy, at least formally,

$$A_j = z_{ji} \otimes A_i \quad (A5)$$

We found, as did van der Marel (1997), that the functions  $z_{ji}$  can be well approximated by Gaussians with mean velocity  $\widehat{V}_{ji}$  and velocity dispersion  $\widehat{\sigma}_{ji}$ .

### A.3 Kinematical corrections

The functions  $H$  and  $LSF_T$  influence the kinematical analysis for each galaxy spectrum in exactly the same way. Their shape and properties therefore do not enter into the *differences* between the stellar kinematics inferred from observations at different positions  $i$  and  $j$  in the same galaxy. Since the convolution of two Gaussians is again a Gaussian, it is straightforward to show that

$$V_j - V_i = \widetilde{V}_j - \widetilde{V}_i + \widehat{V}_{ji} \quad (A6)$$

and

$$\sigma_j^2 - \sigma_i^2 = \widetilde{\sigma}_j^2 - \widetilde{\sigma}_i^2 + \widehat{\sigma}_{ji}^2. \quad (A7)$$

So if the stellar kinematics for any galaxy spectrum  $j$  are known *a priori*, then the kinematics at any other position  $i$  can be calculated without knowledge of either of the functions  $H$  and  $LSF_T$ .

### A.4 Reference kinematics

Position #5 for each galaxy is located at  $\sim 0.5''$  from the galaxy center (cf. see Table 5). This position is beyond the region most affected by seeing in ground-based observations, and can therefore be used as a ‘reference position’ for use with equations (A6) and (A7). One possibility is to assume that the velocity dispersions for spectra A5 and B5 are known *a priori*, from the results of the ground-based WHT

observations. This yields  $\sigma_5 = 260.7 \text{ km s}^{-1}$  for NGC 4342, and  $\sigma_5 = 173.1 \text{ km s}^{-1}$  for NGC 4570. More accurate estimates for  $\sigma_5$  can be obtained by modeling the small residual effect of seeing on the ground-based observations. For this purpose we calculated predicted kinematical quantities from  $f(E, L_z)$  Jeans equation models for the ground-based kinematics, based on the MGE-fitted density distributions (see Cretton & van den Bosch 1997). We then calculated predictions for  $\sigma_5$ , by convolving the unconvolved model kinematics with the  $0.26''$  aperture kernel at the appropriate positions. This yielded  $\sigma_5 = 237.5 \text{ km s}^{-1}$  and  $\sigma_5 = 170.8 \text{ km s}^{-1}$  for NGC 4342 and NGC 4570 respectively. Comparison with the directly observed values confirms that the effect of seeing convolution at a galactocentric distance of  $0.5''$  is only modest.

The LSF corrected stellar kinematics listed in Table 5 were obtained using equations (A6) and (A7), with the seeing corrected  $\sigma_5$  as reference value, and with  $\widehat{V}_{i5}$  and  $\widehat{\sigma}_{i5}$  chosen so as to best fit equation (A5). The systemic velocity was independently estimated and subtracted from the velocities as described in Section 5.2. Hence, any arbitrary value may be used for the reference velocity  $V_5$ , because it only enters into equation (A6) as an additive constant.

### A.5 Consistency check

As a consistency check on the *assumed* values of  $\sigma_5$ , we also tried to *calculate*  $\sigma_5$  from the actual FOS observations. This can be done under the assumption that the LSFs of both the galaxy and template spectrum are Gaussian, with dispersions  $\sigma_G$  and  $\sigma_T$ , respectively. This is not a very accurate approximation, but provides a useful consistency check. It yields:

$$\sigma_5^2 = \widetilde{\sigma}_5^2 + \sigma_T^2 - \sigma_G^2. \quad (\text{A8})$$

The dispersion of the template spectrum is  $\sigma_T = 71 \text{ km s}^{-1}$  (at  $5170\text{\AA}$ ), whereas  $\sigma_G = 100 \pm 2 \text{ km s}^{-1}$  (Keyes et al. 1995). The dispersions  $\widetilde{\sigma}_5$  measured directly from the  $\chi^2$  minimization (A3) are  $240.6 \text{ km s}^{-1}$  and  $171.5 \text{ km s}^{-1}$ , for NGC 4342 and NGC 4570, respectively. This yields with equation (A8) that  $\sigma_5 = 230.1 \text{ km s}^{-1}$  for NGC 4342, and  $\sigma_5 = 156.4 \text{ km s}^{-1}$  for NGC 4570, in good agreement (within the error bars of the FOS data) with the values derived from the Jeans modeling. The reference values assumed on the basis of modeling of the ground-based data are therefore confirmed by the FOS data.

### A.6 Analysis with an HST template

As yet another test, we also analyzed the FOS spectra with an actual FOS template spectrum: the KIII star F193, observed with the same instrumental setup as our galaxy spectra. There is definite template mismatch between this stellar spectrum and our galaxy spectra, but the results should nonetheless be roughly consistent with those derived using the more appropriate ground-based template.

In this case, the instrumental broadening function  $H$  (equation [A4]) is the same for the galaxy and template spectra. However, the template has a different illumination function  $A_T$  than the galaxy spectra. We calculated  $A_T$  assuming that the star was properly centred in the  $0.26''$  aperture. In analogy with equation (A5), we subsequently

**Table A1.** HST/FOS stellar kinematics: a consistency check

NGC 4342			NGC 4570		
id.	$\delta_V$	$\delta_\sigma$	id.	$\delta_V$	$\delta_\sigma$
A1	-0.73	-0.41	B1	-1.29	+0.52
A2	+0.41	-0.39	B2	-0.14	-0.38
A3	-0.55	+0.93	B3	+0.06	+0.59
A4	-0.32	+0.02	B4	-2.01	+0.26
A5	+0.68	+0.76	B5	-2.85	-1.24
A6	-0.26	-0.50	B6	-0.54	-0.28
A7	-0.32	+0.33	B7	-1.51	-1.06

The quantities  $\delta_V$  and  $\delta_\sigma$  are the differences between the kinematical results obtained from the HST/FOS galaxy spectra with: (a) a ground-based template that provides a good match to the galaxy spectra; and (b) an HST template that has significant template mismatch. The differences are expressed in units of the formal error bars.

assumed that each  $A_i$  can be approximated as a convolution of  $A_T$  with a Gaussian. For each galaxy spectrum we found the best Gaussian, and convolved it with the template spectrum. This results in a different template spectrum for each galaxy spectrum, that has the same LSF as the galaxy spectrum. We refer to the stellar kinematics determined with these templates as  $V_i^*$  and  $\sigma_i^*$ . In Table A1 we list the relative differences  $\delta_V \equiv (V_i^* - V_i)/\Delta V_i$  and  $\delta_\sigma \equiv (\sigma_i^* - \sigma_i)/\Delta \sigma_i$ , between these results and those listed in Table 5. The agreement is satisfactory: most residuals are smaller than the error bars listed in Table 5 (i.e.,  $\delta < 1$ ). The results in Table 5 are the more accurate ones, because they suffer less from template mismatch.

The results obtained with an HST template are consistent with those derived using a ground-based template. This confirms that there are no large systematic errors in our analysis.

## APPENDIX B: WHT KINEMATICS

The tables in this Appendix list the stellar kinematics inferred from the WHT spectra. The quantities  $V$  and  $\sigma$  (in  $\text{km s}^{-1}$ ) are the mean and dispersion of best-fitting Gaussian VPs, and  $h_3$  and  $h_4$  are the lowest-order Gauss-Hermite moments of the VPs. The kinematics inferred from the HST/FOS spectra are listed in Table 5.

This paper has been produced using the Blackwell Scientific Publications  $\text{\TeX}$  macros.

**Table B1.** NGC 4342 major axis

R	V	$\Delta V$	$\sigma$	$\Delta\sigma$	$h_3$	$\Delta h_3$	$h_4$	$\Delta h_4$
-14.235	-238.5	9.4	94.6	12.1	-0.111	0.088	0.041	0.070
-11.218	-223.6	6.3	78.6	7.7	-0.040	0.068	-0.038	0.056
-9.463	-233.1	7.0	95.8	9.6	0.042	0.068	0.037	0.054
-8.222	-231.1	8.8	118.0	11.6	-0.052	0.070	0.035	0.055
-7.147	-216.7	6.5	100.2	9.1	-0.003	0.061	0.051	0.048
-6.259	-227.8	8.4	109.8	11.0	0.093	0.072	0.003	0.057
-5.542	-212.2	8.3	117.9	10.6	-0.062	0.066	0.007	0.052
-4.826	-204.2	8.3	144.1	11.9	0.114	0.056	0.042	0.044
-4.109	-190.2	7.3	129.4	8.8	0.078	0.050	-0.016	0.040
-3.580	-155.8	9.3	126.5	11.9	0.059	0.065	0.029	0.053
-3.222	-145.9	10.3	152.3	13.8	0.055	0.061	0.038	0.050
-2.864	-152.3	9.5	134.9	12.7	-0.011	0.063	0.046	0.052
-2.506	-141.1	9.5	165.3	11.1	-0.043	0.049	-0.025	0.039
-2.148	-137.6	10.0	180.0	13.4	-0.049	0.050	0.024	0.040
-1.790	-123.6	9.4	183.8	12.8	-0.057	0.046	0.031	0.036
-1.432	-114.9	10.1	220.5	12.8	0.001	0.038	0.010	0.031
-1.074	-135.0	6.9	196.3	9.2	-0.008	0.031	0.025	0.025
-0.716	-124.6	7.4	243.5	9.8	0.071	0.026	-0.011	0.021
-0.358	-71.2	7.7	292.9	10.6	0.046	0.022	-0.012	0.018
0.000	0.0	7.3	317.1	10.6	-0.026	0.021	-0.015	0.016
0.358	70.5	7.0	276.8	9.5	-0.050	0.021	-0.007	0.017
0.716	114.2	7.1	215.3	9.5	-0.011	0.027	0.006	0.022
1.074	134.1	7.3	197.1	9.3	0.002	0.030	-0.016	0.025
1.432	132.8	8.0	175.1	10.9	0.045	0.038	0.017	0.032
1.790	120.4	8.8	160.5	11.4	0.041	0.046	0.002	0.038
2.148	124.2	8.7	152.2	11.1	-0.042	0.047	0.006	0.040
2.506	154.8	8.9	147.9	11.1	0.032	0.050	-0.020	0.042
2.864	153.3	10.1	147.0	12.2	-0.062	0.056	-0.012	0.047
3.222	158.6	9.3	139.1	11.2	-0.039	0.055	-0.016	0.045
3.580	158.3	10.1	135.9	12.5	-0.008	0.063	-0.014	0.052
4.109	178.7	6.8	121.0	9.1	-0.094	0.050	0.020	0.041
4.826	189.7	6.6	101.2	9.2	-0.123	0.059	0.040	0.047
5.542	197.2	7.6	108.1	9.3	-0.041	0.060	-0.024	0.048
6.429	197.8	7.1	113.1	8.1	-0.045	0.052	-0.055	0.042
7.505	203.9	6.8	90.0	8.0	-0.130	0.063	-0.053	0.051
8.749	207.4	6.3	90.4	7.9	-0.043	0.061	-0.034	0.049
10.344	219.8	6.5	81.4	7.9	-0.112	0.066	-0.024	0.055
12.614	214.5	7.1	90.0	8.8	0.010	0.067	-0.028	0.055

**Table B2.** NGC 4342 minor axis

R	V	$\Delta V$	$\sigma$	$\Delta\sigma$	$h_3$	$\Delta h_3$	$h_4$	$\Delta h_4$
-2.661	15.2	9.9	107.4	13.3	0.138	0.079	0.044	0.064
-2.148	-3.7	15.1	190.4	25.5	-0.092	0.068	0.133	0.056
-1.790	-6.2	12.3	200.4	16.4	-0.035	0.052	0.019	0.043
-1.432	16.8	9.1	183.8	13.0	-0.027	0.044	0.028	0.036
-1.074	5.0	9.3	219.5	10.9	0.036	0.033	-0.031	0.028
-0.716	-5.8	7.1	240.9	9.6	0.017	0.027	-0.034	0.022
-0.358	-0.8	6.9	299.0	10.1	0.048	0.021	-0.008	0.016
0.000	0.0	6.2	293.3	9.5	0.056	0.020	-0.012	0.016
0.358	-3.7	6.6	265.5	9.5	0.054	0.022	0.009	0.018
0.716	-10.7	6.9	239.4	10.1	0.047	0.025	0.028	0.021
1.074	-1.7	7.1	216.7	9.9	0.013	0.029	0.007	0.024
1.432	6.4	8.6	191.2	11.0	-0.048	0.037	0.006	0.031
1.790	9.0	9.1	156.1	12.0	-0.051	0.049	0.025	0.041
2.148	20.7	9.8	138.5	12.3	-0.059	0.060	-0.013	0.050
2.658	37.9	8.4	114.3	10.8	-0.007	0.065	-0.011	0.052

**Table B3.** NGC 4570 major axis

R	V	$\Delta V$	$\sigma$	$\Delta\sigma$	$h_3$	$\Delta h_3$	$h_4$	$\Delta h_4$
-33.516	-161.3	4.4	71.4	6.2	0.051	0.051	0.037	0.044
-26.363	-157.4	4.7	86.6	6.6	0.061	0.048	0.001	0.039
-21.951	-165.5	4.3	84.3	6.6	-0.065	0.048	-0.003	0.039
-18.749	-158.6	4.5	88.2	5.9	0.093	0.043	-0.024	0.034
-16.259	-148.2	5.0	99.2	6.7	0.133	0.044	-0.016	0.035
-14.308	-127.7	6.1	113.8	7.9	0.025	0.045	-0.006	0.036
-12.518	-118.5	5.5	108.1	6.6	-0.012	0.042	-0.045	0.033
-10.907	-114.0	5.1	95.1	7.1	0.029	0.047	0.003	0.038
-9.472	-96.3	5.4	118.7	7.2	0.014	0.039	-0.016	0.032
-8.222	-83.5	5.5	113.9	7.1	-0.066	0.041	-0.025	0.034
-7.144	-91.2	5.3	118.2	8.2	0.029	0.041	0.037	0.034
-6.258	-90.6	6.1	112.9	8.2	-0.030	0.047	-0.017	0.038
-5.542	-96.7	5.7	131.7	7.2	0.081	0.036	-0.036	0.030
-4.825	-95.4	5.2	130.8	6.5	0.014	0.033	-0.038	0.028
-4.296	-81.6	7.2	142.8	9.4	-0.028	0.042	-0.036	0.035
-3.938	-85.8	7.0	149.1	9.4	0.010	0.038	-0.012	0.032
-3.580	-88.5	6.7	149.1	9.0	0.005	0.037	-0.019	0.031
-3.222	-86.3	6.5	141.2	9.0	-0.018	0.039	0.009	0.033
-2.864	-74.9	6.4	147.5	8.4	-0.090	0.036	-0.033	0.030
-2.506	-75.1	5.8	157.1	7.4	-0.032	0.030	-0.041	0.025
-2.148	-66.1	5.5	158.6	7.4	0.017	0.028	-0.016	0.024
-1.790	-64.6	5.1	161.8	7.0	0.018	0.026	-0.014	0.022
-1.432	-59.2	4.6	167.8	6.7	0.018	0.023	-0.007	0.019
-1.074	-43.2	4.0	161.9	5.6	-0.003	0.021	-0.006	0.017
-0.716	-33.6	4.1	178.4	5.8	0.003	0.019	-0.011	0.015
-0.358	-15.7	4.0	193.0	5.9	-0.001	0.017	-0.012	0.014
0.000	0.0	3.9	197.8	5.8	-0.019	0.016	-0.018	0.013
0.358	8.6	4.0	197.6	5.8	-0.018	0.017	-0.030	0.014
0.716	32.3	4.1	189.3	6.0	-0.039	0.018	-0.018	0.015
1.074	50.9	4.5	186.9	6.2	-0.047	0.020	-0.020	0.016
1.432	62.6	4.8	180.3	6.9	-0.069	0.022	-0.006	0.018
1.790	63.8	5.2	171.8	7.2	-0.014	0.025	-0.002	0.020
2.148	68.1	5.6	164.2	8.0	-0.045	0.029	-0.007	0.024
2.506	77.8	6.2	159.6	8.4	-0.061	0.032	-0.015	0.026
2.864	90.7	5.8	152.1	7.8	-0.039	0.032	-0.012	0.027
3.222	100.0	6.5	147.4	8.3	-0.049	0.036	-0.012	0.030
3.580	91.3	7.5	164.0	10.2	-0.024	0.037	-0.009	0.031
3.938	101.5	7.8	161.2	10.3	0.024	0.039	-0.018	0.033
4.296	101.4	7.7	153.6	9.7	0.006	0.040	-0.041	0.034
4.825	100.0	5.6	154.5	7.1	0.019	0.029	-0.039	0.024
5.541	82.6	6.0	135.8	7.9	0.040	0.037	-0.010	0.031
6.258	88.4	6.2	133.5	8.1	-0.037	0.038	-0.005	0.032
7.145	97.4	5.2	115.9	6.7	-0.013	0.039	-0.024	0.032
8.223	85.1	6.0	117.6	8.8	-0.019	0.046	0.027	0.037
9.470	80.6	5.4	122.7	7.4	-0.005	0.038	-0.002	0.031
10.909	104.2	5.3	95.0	7.3	0.002	0.048	0.017	0.038
12.517	119.8	4.5	98.7	5.2	0.000	0.037	-0.069	0.029
14.303	128.3	4.9	102.3	5.7	-0.057	0.039	-0.046	0.031
16.266	152.4	4.9	86.5	5.5	-0.072	0.046	-0.091	0.037
18.755	148.4	5.2	90.6	6.2	-0.167	0.047	-0.045	0.038
21.948	152.1	5.2	88.1	5.7	-0.050	0.046	-0.099	0.037
26.375	176.4	4.3	83.1	7.1	-0.095	0.046	0.064	0.038
33.529	161.8	4.6	83.4	5.5	0.034	0.045	-0.078	0.037

**Table B4.** NGC 4570 offset axis

R	V	$\Delta V$	$\sigma$	$\Delta\sigma$	$h_3$	$\Delta h_3$	$h_4$	$\Delta h_4$
-32.931	-182.6	4.6	68.5	5.5	-0.046	0.046	0.022	0.040
-25.097	-155.7	5.0	96.9	6.9	0.051	0.043	0.034	0.035
-20.515	-147.1	4.3	90.5	5.8	0.142	0.041	0.002	0.033
-17.318	-145.0	4.3	99.9	6.5	-0.054	0.040	0.027	0.032
-14.835	-128.6	4.6	107.3	6.1	-0.006	0.039	-0.025	0.031
-12.874	-121.6	5.2	111.3	6.0	-0.051	0.039	-0.060	0.031
-11.080	-92.7	5.1	106.5	6.0	-0.162	0.039	-0.038	0.031
-9.471	-92.7	5.0	120.9	6.8	-0.055	0.038	-0.020	0.031
-8.222	-71.1	5.7	107.2	6.8	-0.104	0.045	-0.037	0.036
-7.146	-73.8	5.1	102.8	6.8	-0.072	0.043	-0.006	0.034
-6.259	-90.8	6.6	127.4	7.6	-0.012	0.041	-0.050	0.034
-5.542	-85.9	5.9	138.3	7.6	0.030	0.036	-0.051	0.030
-4.825	-76.3	5.3	120.6	6.8	0.023	0.037	-0.013	0.030
-4.109	-78.4	4.8	132.3	6.4	0.000	0.031	-0.010	0.026
-3.580	-71.8	6.8	135.6	8.9	0.063	0.042	-0.017	0.035
-3.222	-60.1	7.0	147.2	8.4	0.007	0.038	-0.054	0.032
-2.864	-62.4	6.6	147.3	8.4	-0.022	0.037	-0.036	0.031
-2.506	-60.5	6.5	161.9	8.9	-0.023	0.033	0.000	0.027
-2.148	-58.5	6.5	163.3	9.1	-0.038	0.033	-0.007	0.027
-1.790	-47.3	5.7	149.8	8.0	-0.026	0.033	-0.012	0.028
-1.432	-40.1	5.8	159.6	8.3	-0.025	0.031	-0.003	0.026
-1.074	-30.7	5.5	165.8	7.8	0.013	0.028	-0.006	0.023
-0.716	-23.3	5.4	175.2	7.5	0.002	0.025	-0.012	0.021
-0.358	-5.7	5.4	176.9	7.9	-0.015	0.026	0.000	0.021
0.000	0.0	5.4	172.2	8.1	-0.033	0.026	0.019	0.022
0.358	16.0	5.0	165.9	7.6	-0.047	0.026	0.013	0.022
0.716	26.2	5.4	175.7	7.9	-0.048	0.026	0.001	0.021
1.074	34.9	5.6	174.3	8.2	-0.028	0.027	0.001	0.022
1.432	45.9	5.9	173.5	8.3	-0.039	0.028	-0.005	0.023
1.790	62.2	6.0	163.4	8.3	-0.048	0.030	-0.003	0.025
2.148	70.7	6.0	154.0	8.4	-0.028	0.033	-0.005	0.028
2.506	72.6	6.0	145.8	7.9	-0.029	0.034	-0.022	0.029
2.864	78.4	6.6	148.3	8.5	0.001	0.037	-0.036	0.031
3.222	76.1	6.5	141.4	8.7	0.012	0.039	-0.015	0.033
3.580	81.7	6.9	143.7	9.1	-0.019	0.040	-0.013	0.033
4.109	89.0	5.1	146.6	7.4	-0.068	0.031	0.013	0.026
4.826	94.5	5.5	136.4	7.1	-0.055	0.034	-0.013	0.028
5.542	92.6	5.6	127.1	7.3	0.031	0.038	-0.013	0.031
6.259	94.5	6.5	129.3	8.7	-0.018	0.042	0.010	0.035
7.146	99.7	5.6	126.9	7.4	-0.074	0.037	0.003	0.031
8.223	108.9	6.2	121.3	7.9	-0.005	0.045	-0.040	0.037
9.472	97.2	5.0	96.2	7.2	0.044	0.046	0.030	0.037
11.080	126.1	5.6	106.1	6.7	0.091	0.045	-0.055	0.036
12.870	137.5	5.3	99.6	6.9	0.022	0.046	-0.022	0.037
14.841	144.7	5.1	115.5	6.1	-0.001	0.038	-0.067	0.030
17.316	158.0	4.7	100.6	5.7	-0.061	0.038	-0.031	0.031
20.516	176.3	4.2	87.7	5.8	-0.091	0.041	-0.008	0.033
25.086	176.7	3.4	73.9	5.1	-0.136	0.043	-0.020	0.036
32.870	179.2	3.6	70.0	4.7	-0.082	0.043	-0.035	0.037

**Table B5.** NGC 4570 minor axis

R	V	$\Delta V$	$\sigma$	$\Delta\sigma$	$h_3$	$\Delta h_3$	$h_4$	$\Delta h_4$
-5.430	8.4	6.5	125.1	8.0	-0.010	0.043	-0.031	0.035
-3.903	18.4	6.7	121.5	8.9	0.025	0.048	-0.010	0.039
-3.027	10.5	7.1	138.6	9.4	-0.066	0.043	-0.020	0.036
-2.308	-2.1	6.5	156.6	9.1	-0.022	0.034	0.007	0.029
-1.790	-1.8	7.8	170.5	11.1	-0.043	0.037	-0.002	0.031
-1.432	-1.3	7.3	185.9	10.9	0.003	0.032	0.006	0.027
-1.074	-10.7	6.6	201.8	10.5	0.006	0.027	0.015	0.022
-0.716	-5.5	5.8	189.5	8.8	0.018	0.025	0.003	0.021
-0.358	-4.7	5.6	184.3	8.3	-0.016	0.025	-0.004	0.021
0.000	0.0	5.7	184.0	8.4	-0.039	0.025	-0.004	0.021
0.358	3.1	5.8	190.6	8.7	0.003	0.025	-0.005	0.021
0.716	-0.2	5.8	187.0	8.1	0.032	0.025	-0.020	0.021
1.074	-3.5	6.3	176.6	9.1	0.019	0.030	-0.003	0.025
1.432	-1.8	7.1	183.6	11.7	0.001	0.033	0.029	0.027
1.790	3.5	8.1	178.4	14.0	-0.041	0.039	0.043	0.032
2.148	13.6	8.0	136.0	11.1	0.006	0.053	-0.017	0.044
2.668	12.0	6.5	149.0	9.6	0.004	0.037	0.014	0.032
3.543	18.5	6.5	138.3	9.2	-0.066	0.040	0.009	0.034
4.922	22.2	6.2	116.2	8.6	-0.062	0.048	-0.003	0.039
8.059	9.6	6.6	106.5	9.7	-0.019	0.054	0.043	0.043